PHYSICAL REVIEW D **83,** 024007 (2011)

N-body simulations for coupled scalar-field cosmology

Baojiu Li[1,2,*] and John D. Barrow[1,†]

[1]*DAMTP, Centre for Mathematical Sciences, University of Cambridge, Wilberforce Road, Cambridge CB3 0WA, United Kingdom*
[2]*Kavli Institute for Cosmology Cambridge, Madingley Road, Cambridge CB3 0HA, United Kingdom*

(Received 20 May 2010; published 7 January 2011)

We describe in detail the general methodology and numerical implementation of consistent N-body simulations for coupled-scalar-field models, including background cosmology and the generation of initial conditions (with the different couplings to different matter species taken into account). We perform fully consistent simulations for a class of coupled-scalar-field models with an inverse power-law potential and negative coupling constant, for which the chameleon mechanism does not work. We find that in such cosmological models the scalar-field potential plays a negligible role except in the background expansion, and the fifth force that is produced is proportional to gravity in magnitude, justifying the use of a rescaled gravitational constant G in some earlier N-body simulation works for similar models. We then study the effects of the scalar coupling on the nonlinear matter power spectra and compare with linear perturbation calculations to see the agreement and places where the nonlinear treatment deviates from the linear approximation. We also propose an algorithm to identify gravitationally virialized matter halos, trying to take account of the fact that the virialization itself is also modified by the scalar-field coupling. We use the algorithm to measure the mass function and study the properties of dark-matter halos. We find that the net effect of the scalar coupling helps produce more heavy halos in our simulation boxes and suppresses the inner (but not the outer) density profile of halos compared with the ΛCDM prediction, while the suppression weakens as the coupling between the scalar field and dark-matter particles increases in strength.

DOI: 10.1103/PhysRevD.83.024007 PACS numbers: 04.50.Kd

I. INTRODUCTION

One of the most challenging questions in modern physics is the origin and nature of dark energy [1], which dominates the present energy budget of our Universe. Although a cosmological constant could fit most current observations, it suffers from the fine-tuning and coincidence problems, which makes it less appealing theoretically. Amongst the alternative theories, those involving scalar fields are most popular. The simplest is the so-called quintessence scenario [2–4], employing a scalar field which slowly rolls down its potential when its potential energy dominates over kinetic energy, resulting in an equation of state with a pressure-density ratio close to -1. The quintessence field is generally very light and barely clusters so that its effect in cosmology is mainly through its modification of the background expansion rate. A more complicated but phenomenologically interesting possibility is that the scalar field couples to (some of) the matter species, which might somehow alleviate the coincidence problem [5]. These coupled-scalar-field models have attracted much recent interest (see, for example, [6–13] and references there in).

A coupling between matter to the scalar field, however, raises serious problems for the viability of the theory. It is well known that the fifth force arising from any such a coupling should be very weak or very short ranged if it is not to violate direct experimental constraints. Some specially contrived mechanisms have been proposed to prevent such contradictions, such as the chameleon [14,15] and the environment-dependent dilaton [16] models, where the fifth force is designed to be suppressed in high-density regions. A simpler approach is to have the scalar field coupling to dark matter only, which means that laboratory and solar-system constraints on the fifth force are inapplicable. Such an idea has attracted much recent interest (e.g., [17–19]). In this work we shall consider such a situation, and for a chameleonlike scalar field similar studies have been conducted by [20–22].

The formation of cosmological structure in the presence of coupled scalar fields at the linear perturbative level has already been studied in great detail. Here, we extend these studies into the nonlinear regime. In particular, we want to know how structure formation on the scales of galaxies and galaxy clusters is modified. As we shall see below, there are principally four effects of the scalar-field coupling, namely, through (i) the modification of the background expansion rate, (ii) the action of a fifth force on dark-matter particles, (iii) the reduced contribution of dark matter to the Poisson equation, and (iv) the change of the initial condition at early times. Of these four, (ii) can actually be subdivided into (a) an essential "rescaling" of gravitational constant and (b) a velocity-dependent acceleration term, while (iv) is a combined consequence of (i, ii, iii) before $z \sim 50$. We cannot track all of these effects into the nonlinear regime

*b.li@damtp.cam.ac.uk
†j.d.barrow@damtp.cam.ac.uk

using linear analysis and the tool we will employ to obtain quantitative predictions is N-body simulation [23].

There has been some earlier work in this area (see, for example, [24–35] and also [36–41] for related works). However, in all of those scalar-field simulations the scalar-field equation is not solved explicitly, but rather it is assumed either that the fifth force is proportional to gravity so that its effect is a simple rescaling of the gravitational constant, or that the fifth force takes the Yukawa form with exponential cutoff beyond some scale. On the other hand, the recent fully consistent simulations performed in [20–22] have shown that, at least for the chameleon scalar-field models, the above simplifying approximations are not good and raises questions about the extent to which we should trust them. These concerns motivate this paper, in which we test the accuracy of those approximations and study in more detail the qualitative and quantitative effects of a coupled scalar field on the formation and evolution of the nonlinear cosmic structure.

As in [22,30], we shall consider a universe which at late times is dominated by a scalar field and two matter species, namely, the dark matter, which couples to the scalar field in a way prescribed in Sec. II A and the so-called "baryons," which are essentially the dark matter *without* scalar-field coupling.

The paper is organized as follows: in Sec. II we list the essential equations to be implemented by our N-body simulations and describe briefly their differences from standard ΛCDM. Section III presents a comprehensive description of the methodology used in this paper and its implementation in the numerical code. Section III A lists the physical and simulation parameters we adopt; Sec. III B illustrates how we distinguish between baryons and dark-matter particles; Sec. III C summarizes the results for the background expansion and linear perturbation evolution, which will be referred to subsequently from time to time; and finally Sec. III D and Appendix D explain in detail how to generate initial conditions for the N-body simulations which take into account the effects of the coupling between dark matter and the scalar field. As we aim to set up a general framework for N-body simulations of coupled-scalar-field models, we have tried to include all the main ingredients in this section. Our numerical results are presented in Sec. IV, within which Sec. IV A displays some general results, showing that the approximation of rescaling gravitational constant as used in previous literature is a very good one for the model studied here (but not necessarily so for other models), and Secs. IV B, IV C, and IV D discuss, respectively, how the coupling modifies the nonlinear matter power spectrum, mass function, and the internal density profiles of halos. We present our conclusions in Sec. VI.

Throughout the paper a subscript B (D) denotes a corresponding quantity for baryons (dark matter), unless otherwise stated.

II. THE EQUATIONS

The equations that will be used in the N-body simulations have been discussed in detail in Refs. [20,22]. As we are considering a qualitatively different model here, and the parametrization and discretization of equations are both different, we list these equations and discuss them for completeness.

A. The basic equations

The Lagrangian for our model is

$$\mathcal{L} = \frac{1}{2}\left[\frac{R}{\kappa} - \nabla^a\varphi\nabla_a\varphi\right] + V(\varphi) - C(\varphi)\mathcal{L}_{\rm CDM} + \mathcal{L}_{\rm S}, \quad (1)$$

where R is the Ricci scalar, $\kappa = 8\pi G$, with G Newton's constant, φ is the scalar field, $V(\varphi)$ its potential energy, and $C(\varphi)$ its coupling to the (cold) dark matter described by the Lagrangian density $\mathcal{L}_{\rm CDM}$; $\mathcal{L}_{\rm S}$ includes standard model fields/particles. The contribution from photons and neutrinos in the N-body simulations [$z \sim \mathcal{O}(10) \sim \mathcal{O}(1)$] is negligible, but it does have effects on the matter power spectrum at redshift $z \sim 50$, through the early evolution of the Universe (see Sec. III D and Appendix D), and so we have included it in the linear perturbation computation.

The dark-matter Lagrangian for a pointlike particle with (bare) mass m_0 is

$$\mathcal{L}_{\rm CDM}(\mathbf{y}) = -\frac{m_0}{\sqrt{-g}}\delta(\mathbf{y}-\mathbf{x}_0)\sqrt{g_{ab}\dot{x}_0^a\dot{x}_0^b}, \quad (2)$$

where $\mathbf{y}$ is the general coordinate and $\mathbf{x}_0$ is the coordinate of the center of the particle. The energy-momentum tensor for dark matter can be derived from this equation as

$$T^{ab}_{\rm CDM} = \frac{m_0}{\sqrt{-g}}\delta(\mathbf{y}-\mathbf{x}_0)\dot{x}_0^a\dot{x}_0^b. \quad (3)$$

Also, because $g_{ab}\dot{x}_0^a\dot{x}_0^b \equiv g_{ab}u^a u^b = 1$, with u^a the four-velocity of the dark-matter particle that is centered at x_0, Eq. (2) can be simplified as

$$\mathcal{L}_{\rm CDM}(\mathbf{y}) = -\frac{m_0}{\sqrt{-g}}\delta(\mathbf{y}-\mathbf{x}_0), \quad (4)$$

which will be used in the derivation of the scalar-field equation of motion (see Appendix B).

For a fluid with many particles, the energy-momentum tensor can be obtained by spatial averaging of Eq. (3), which is for a single particle, and we get

$$\begin{aligned} T^{ab}_{\rm CDM} &= \frac{1}{\mathcal{V}}\int_{\mathcal{V}} d^4y\sqrt{-g}\frac{m_0}{\sqrt{-g}}\delta(y-x_0)\dot{x}_0^a\dot{x}_0^b \\ &= \rho_{\rm CDM}u^a u^b, \end{aligned} \quad (5)$$

in which $\mathcal{V}$ is a microscopically large but macroscopically small volume, and the 3-dimensional δ function has been extended to a 4-dimensional one by adding a time component. Here, u^a is the averaged four-velocity of the dark-matter fluid, which is *not* necessarily the same as the four-velocity of the observer, as will be discussed below.

Using

$$T^{ab} = -\frac{2}{\sqrt{-g}}\frac{\delta(\sqrt{-g}\mathcal{L})}{\delta g_{ab}}, \tag{6}$$

The total energy-momentum tensor is derived as

$$\begin{aligned} T_{ab} &= \nabla_a\varphi\nabla_b\varphi - g_{ab}[\tfrac{1}{2}\nabla_c\varphi\nabla^c\varphi - V(\varphi)] \\ &\quad + C(\varphi)T^{\mathrm{CDM}}_{ab} + T^{\mathrm{S}}_{ab} \end{aligned} \tag{7}$$

where $T^{\mathrm{CDM}}_{ab} = \rho_{\mathrm{CDM}}u_a u_b$, T^{S}_{ab} is the energy-momentum tensor for standard model particles, and the Einstein equations are, as usual,

$$G_{ab} = \kappa T_{ab} \tag{8}$$

where G_{ab} is the Einstein tensor. Note that the coupling between the scalar field and the dark matter ensures that the energy-momentum tensors for both will not be conserved separately; instead, we have

$$\nabla_b T^{\mathrm{CDM}ab} = -\frac{C_\varphi(\varphi)}{C(\varphi)}(g^{ab}\mathcal{L}_{\mathrm{CDM}} + T^{\mathrm{CDM}ab})\nabla_b\varphi, \tag{9}$$

where throughout this paper we shall use subscript φ to denote a derivative with respect to φ. However, the total energy-momentum tensor of the two is conserved.

Finally, the scalar-field equation of motion is given as [20]

$$\Box\varphi + \frac{\partial V(\varphi)}{\partial\varphi} + \rho_{\mathrm{CDM}}\frac{\partial C(\varphi)}{\partial\varphi} = 0 \tag{10}$$

where we have used Eq. (4).

Equations (7)–(10) summarize all of the physics needed for the following analysis.

We will consider an inverse power-law potential energy for the scalar field,

$$V(\varphi) = \frac{\Lambda^4}{(\sqrt{\kappa}\varphi)^\alpha}, \tag{11}$$

where α is a dimensionless constant and Λ is a constant with dimensions of mass. This potential has been very popular in various background or linear perturbation studies of scalar fields (either minimally or nonminimally coupled); the tracking behavior it produces makes it a good dark-energy candidate and for that purpose we shall choose $\alpha \sim \mathcal{O}(0.1\text{–}1)$. As we shall see below, our choices of parameters mean that this potential makes the scalar field a nonchameleonic one, which is qualitatively different from [20,22]. In some sense, the studies in this work and [20,22] represent two extremes of the scalar-field behavior, with the scalar field strongly (barely) clustering there (here), and when combined these studies give a fuller understanding of the complexity of coupled scalar fields. In addition, our choice of potential in Eq. (11), which is the same as most previous studies, enables us to test the validity of the approximations used there.

Meanwhile, the coupling between the scalar field and dark-matter particles is chosen as

$$C(\varphi) = \exp(\gamma\sqrt{\kappa}\varphi), \tag{12}$$

where $\gamma < 0$ is another dimensionless constant characterizing the strength of the coupling. As we shall see below, $2|\gamma|^2$ is roughly the ratio of the magnitudes of the fifth force and gravity on the dark-matter particles.

The bare potential Eq. (11) and the coupling function Eq. (12) form an effective total potential

$$V_{\mathrm{eff}}(\varphi) = V(\varphi) + \rho_{\mathrm{CDM}}C(\varphi) \tag{13}$$

for the scalar field φ, just as in [20,22]. However, both $V(\varphi)$ and $C(\varphi)$ decrease as φ increases here, there is no finite global minimum for $V_{\mathrm{eff}}(\varphi)$, and the scalar field will always continue rolling down the potential given appropriate initial condition. As a result, although in [20,22] the scalar field almost always resides around the minimum of $V_{\mathrm{eff}}(\varphi)$, where it acquires a heavy mass to become a chameleon [14,15], this does not necessarily happen here. Instead, the rolling of the scalar field can be quite rapid, introducing interesting new dynamics in both background cosmology and perturbation evolution.

B. The nonrelativistic limits

The *N*-body simulation only probes the motion of particles at late times, and we are not interested in extreme conditions such as black hole formation and evolution, so that we can take the nonrelativistic limit of the above equations as a good approximation.

As discussed in [22], for the *N*-body simulations for coupled-scalar-field theories, the following equations, or quantities, in their nonrelativistic forms, are needed:

(1) the scalar-field equation of motion, which will be used to compute the value of the scalar field φ at any given time and position;
(2) the Poisson equation, to determine the gravitational potential at any given time and position from the local energy density and pressure;
(3) the total force on dark-matter particles, including the fifth force obtained by differentiating the scalar-field equation solved above.

For the scalar-field equation of motion, we denote by $\bar{\varphi}$ the background value of φ and $\delta\varphi \equiv \varphi - \bar{\varphi}$. Then, in the quasistatic limit where the spatial gradients are much larger than the time derivatives, $|\vec{\nabla}_{\mathbf{r}}\varphi| \gg |\frac{\partial\delta\varphi}{\partial t}|$, the equation for $\delta\varphi$ is given as

$$\begin{aligned} c^2\partial^2_{\mathbf{x}}(a\delta\varphi) &= a^3[V_{,\varphi}(\varphi) - V_{,\varphi}(\bar{\varphi}) + \rho_{\mathrm{CDM}}C_{,\varphi}(\varphi) \\ &\quad - \bar{\rho}_{\mathrm{CDM}}C_{,\varphi}(\bar{\varphi})], \end{aligned} \tag{14}$$

where $\partial^2_{\mathbf{x}} = -\vec{\nabla}^2_{\mathbf{x}} = +(\partial^2_x + \partial^2_y + \partial^2_z)$ is with respect to the comoving coordinate $\mathbf{x} = \mathbf{r}/a$ with $\vec{\nabla}_{\mathbf{x}} = a\vec{\nabla}_{\mathbf{r}}$. For a more detailed derivation see [20,22].

The Poisson equation, in the quasistatic limit and with the contribution from the scalar field taken into account, is shown to be [20,22]

$$\partial_{\mathbf{x}}^2\Phi = 4\pi G a^3[\rho_{\rm CDM}C(\varphi) - \bar{\rho}_{\rm CDM}C(\bar{\varphi})] + 4\pi G a^3 \times[\rho_{\rm B} - \bar{\rho}_{\rm B}] - 8\pi G a^3[V(\varphi) - V(\bar{\varphi})], \quad (15)$$

where Φ is the gravitational potential.

Finally, for the equations of motion of the dark-matter particles, consider Eq. (9). Using Eqs. (3) and (4), this can be reduced to

$$\ddot{x}_0^a + \Gamma^a_{bc}\dot{x}_0^b\dot{x}_0^c = (g^{ab} - u^a u^b)\frac{C_\varphi(\varphi)}{C(\varphi)}\nabla_b\varphi. \quad (16)$$

In this equation, the left-hand side is the conventional geodesic equation of general relativity, and the right-hand side is the new fifth force contribution from the coupling to the scalar field. Note that $g^{ab} - u^a u^b = h^{ab}$ is the projection tensor that projects any 4-tensor into the 3-space perpendicular to u^a, so $(g^{ab} - u^a u^b)\nabla_a = \hat{\nabla}^b$ is the spatial derivative in the 3-space of the observer and perpendicular to u^a. Therefore, the right-hand side of Eq. (16), $\frac{C_\varphi(\varphi)}{C(\varphi)}\hat{\nabla}_a\varphi = \hat{\nabla}_a \log C(\varphi)$, is perpendicular to u^a, which shows that the energy density of dark matter is conserved and only the particle trajectory is modified [20]. As the "observers" are just the individual dark-matter particles [cf. Equation (3)], the force computed above is exactly what those particles feel. The $\delta\varphi$ in Eq. (18) is measured in the dark-matter rest frame while that in Eq. (14) is measured in the fundamental observer's frame. Then, in order to use the $\delta\varphi$ obtained from Eq. (14) in Eq. (16), we need to perform a gauge transformation $\hat{\nabla}_a\varphi \to \hat{\nabla}_a\varphi - \dot{\varphi}v_a$ where v_a is the peculiar velocity of the dark-matter particle relative to the fundamental observer and consequently we will have an additional term $\frac{C_\varphi}{C}\dot{\varphi}v^a$ in Eq. (16), which is the velocity-dependent term identified in [30]. From here on we will always use the $\hat{\nabla}_a\varphi$ measured in the fundamental observer's frame (in which the density perturbation is obtained more directly), and so Eq. (16) should be changed to

$$\ddot{x}_0^a + \Gamma^a_{bc}\dot{x}_0^b\dot{x}_0^c = \frac{C_\varphi(\varphi)}{C(\varphi)}(\hat{\nabla}^a\varphi - \dot{\varphi}v^a). \quad (17)$$

We stress that here

$$v^i = \dot{r}^i = a\dot{x}^i + \dot{a}x^i = a\dot{x}^i \quad (18)$$

where $\dot{r}^i$ is the velocity of a dark-matter particle relative to the fundamental observer which is at the same position at that moment so that $x^i = 0$ but $\dot{x}^i \neq 0$. In the nonrelativistic limit, the spatial components of Eq. (17) can be written as

$$\frac{d^2\mathbf{r}}{dt^2} = -\vec{\nabla}_{\mathbf{r}}\phi - \frac{C_\varphi(\varphi)}{C(\varphi)}\vec{\nabla}_{\mathbf{r}}\varphi - \frac{C_\varphi(\varphi)}{C(\varphi)}a\frac{d(\mathbf{r}/a)}{dt}\dot{\varphi} \quad (19)$$

where t is the physical time coordinate. If we use the comoving coordinate $\mathbf{x}$ instead, then this becomes

$$\ddot{\mathbf{x}} + 2\frac{\dot{a}}{a}\dot{\mathbf{x}} = -\frac{1}{a^3}\vec{\nabla}_{\mathbf{x}}\Phi - \frac{C_\varphi(\varphi)}{C(\varphi)}\left(\frac{1}{a^2}\vec{\nabla}_{\mathbf{x}}\varphi + \dot{\varphi}\,\dot{\mathbf{x}}\right). \quad (20)$$

The canonical momentum conjugate to $\mathbf{x}$ is $\mathbf{p} = a^2\dot{\mathbf{x}}$ so from the equation above we have

$$\frac{d\mathbf{x}}{dt} = \frac{\mathbf{p}}{a^2}, \quad (21)$$

$$\frac{d\mathbf{p}_{\rm CDM}}{dt} = -\frac{1}{a}\vec{\nabla}_{\mathbf{x}}\Phi - \frac{C_\varphi(\varphi)}{C(\varphi)}(\vec{\nabla}_{\mathbf{x}}\varphi + a^2\dot{\varphi}\,\dot{\mathbf{x}}) = -\frac{1}{a}\vec{\nabla}_{\mathbf{x}}\Phi - \frac{C_\varphi(\varphi)}{C(\varphi)}(\vec{\nabla}_{\mathbf{x}}\varphi + \dot{\varphi}\mathbf{p}_{\rm CDM}), \quad (22)$$

$$\frac{d\mathbf{p}_{\rm B}}{dt} = -\frac{1}{a}\vec{\nabla}_{\mathbf{x}}\Phi, \quad (23)$$

where Eq. (22) is for cold dark matter (CDM) particles and Eq. (23) is for baryons. Note that according to Eq. (22) the quantity $a\log[C(\varphi)]$ acts as an effective potential for the fifth force. This is an important observation and we will return to it later when we calculate the escape velocity of CDM particles within a virialized halo.

Equations (14), (15), and (21)–(23) will be used in the code to evaluate the forces on the dark-matter particles and evolve their positions and momenta in time.

C. Code units

In our numerical simulation we use a modified version of MLAPM ([42], see [20,22] for a brief description of the code and the essential modifications to it), and we will have to change or add our Eqs. (14), (15), and (21)–(23). For this, the first step is to convert the quantities to the code units of MLAPM. Here, we briefly summarize the main features.

MLAPM code uses the following internal units (where a subscript c stands for "code"):

$$\mathbf{x}_c = \mathbf{x}/B, \qquad \mathbf{p}_c = \mathbf{p}/(H_0 B) \qquad t_c = tH_0$$
$$\Phi_c = \Phi/(H_0 B)^2 \qquad \rho_c = \rho/\bar{\rho},$$
$$u = ac^2\sqrt{\kappa}\delta\varphi/(H_0 B)^2, \quad (24)$$

where B denotes the comoving size of the simulation box, H_0 is the present Hubble constant, and ρ, with subscript, could represent the density of either CDM ($\rho_{c,\rm CDM}$) or baryons ($\rho_{c,\rm B}$). In the last line the quantity u is the scalar-field *perturbation* $\delta\varphi$ expressed in terms of code units and is new to the MLAPM code.

In terms of u, as well as the (dimensionless) background value of the scalar field, $\sqrt{\kappa}\bar{\varphi}$, some relevant quantities are expressed written in full as

$$V(\varphi) = \frac{\Lambda^4}{(\sqrt{\kappa}\bar{\varphi} + \frac{B^2 H_0^2}{ac^2}u)^{\alpha}},$$

$$C(\varphi) = \exp\left[\gamma\left(\sqrt{\kappa}\bar{\varphi} + \frac{B^2 H_0^2}{ac^2}u\right)\right],$$

$$V_{\varphi} = -\alpha\frac{\sqrt{\kappa}\Lambda^4}{(\sqrt{\kappa}\bar{\varphi} + \frac{B^2 H_0^2}{ac^2}u)^{1+\alpha}},$$

$$C_{\varphi} = \gamma\sqrt{\kappa}\exp\left[\gamma\left(\sqrt{\kappa}\bar{\varphi} + \frac{B^2 H_0^2}{ac^2}u\right)\right], \tag{25}$$

and the background counterparts of these quantities can be obtained simply by setting $u = 0$ (recall that u represents the perturbed part of the scalar field) in the above equations.

Using all the above newly-defined quantities, we can rewrite Eqs. (14), (15), and (21)–(23) as

$$\frac{d\mathbf{x}_c}{dt_c} = \frac{\mathbf{p}_c}{a^2}, \tag{26}$$

$$\frac{d\mathbf{p}_c}{dt_c} = -\frac{1}{a}\nabla\Phi_c\left[-\frac{1}{a}\frac{C_{\varphi}}{\sqrt{\kappa}C}(\nabla u + a\sqrt{\kappa}\dot{\bar{\varphi}}\mathbf{p}_c)\right], \tag{27}$$

$$\nabla^2\Phi_c = \frac{3}{2}\Omega_{\mathrm{CDM}}\bar{C}\left(\rho_{c,\mathrm{CDM}}\frac{C}{\bar{C}} - 1\right) + \frac{3}{2}\Omega_{\mathrm{B}}(\rho_{c,\mathrm{B}} - 1) - \kappa\frac{V - \bar{V}}{H_0^2}a^3, \tag{28}$$

and

$$\nabla^2 u = \frac{3}{\sqrt{\kappa}}\Omega_{\mathrm{CDM}}\bar{C}_{\varphi}\left(\rho_{c\mathrm{CDM}}\frac{C_{\varphi}}{\bar{C}_{\varphi}} - 1\right) + \sqrt{\kappa}\frac{V_{\varphi} - \bar{V}_{\varphi}}{H_0^2}a^3, \tag{29}$$

where $\Omega_{\mathrm{CDM}} = 8\pi G\rho_{\mathrm{CDM}}/3H_0^2$ and $\Omega_{\mathrm{B}} = 8\pi G\rho_{\mathrm{B}}/3H_0^2$ are the dark matter and baryonic fractional energy densities at the present time. Note that in Eq. (27) the term in the brackets on the right-hand side only apply to dark matter and not to baryons. Also note that from here on we shall use $\nabla \equiv \vec{\partial}_{\mathbf{x}_c}$, $\nabla^2 \equiv \vec{\partial}_{\mathbf{x}_c} \cdot \vec{\partial}_{\mathbf{x}_c}$ unless otherwise stated, for simplicity.

We also define

$$\lambda \equiv \frac{\kappa\Lambda^4}{3H_0^2}, \tag{30}$$

which will be used frequently below.

Making discrete versions of the above equations for *N*-body simulations is then straightforward, and we refer the interested readers to Appendix A to the whole treatment, with which we can now proceed to do *N*-body simulations.

III. SIMULATION DETAILS

We have modified the publicly available *N*-body code MLAPM (multilevel adaptive particle mesh) for our simulations. The technical description of the code and our modifications to it are given in [20,22] and interested readers are referred there for more details.

A. Physical and simulation parameters

The physical parameters we use in the simulations are as follows: the present-day dark-energy fractional energy density $\Omega_{\mathrm{DE}} = 0.743$ and $\Omega_m = \Omega_{\mathrm{CDM}} + \Omega_{\mathrm{B}} = 0.257$, $H_0 = 71.9$ km/s/Mpc, $n_s = 0.963$, $\sigma_8 = 0.769$. Our simulation box has a size of $64h^{-1}$ Mpc, where $h = H_0/(100$ km/s/Mpc$)$. We simulate 4 models, with parameters $\alpha = 0.1$ and $\gamma = -0.05$, -0.10, -0.15, -0.20, respectively (such parameters are chosen so that the deviation from ΛCDM will not become too large to be realistic). In all those simulations, the mass resolution is $1.114 \times 10^9 h^{-1} M_{\odot}$; the particle (both dark matter and baryons) number is 256^3 (see Sec. III B for a discussion); the domain grid is a $128 \times 128 \times 128$ cubic, and the finest refined grids have 16 384 cells on each side, corresponding to a force resolution of about $12h^{-1}$ kpc.

We also make a run for the ΛCDM model using the same physical parameters and different initial condition (see Sec. III D).

B. Distinguishing baryons from dark matter

In our simulations only dark-matter particles are coupled to the scalar field. The baryons do not contribute to the scalar-field equation of motion, nor are they influenced by the scalar-field fifth force. Therefore, it is important to make sure that they are distinguished and treated appropriately.

In the modified code we distinguish baryons and dark-matter particles by tagging them differently. This is accomplished using the same algorithm as in [22], but here we consider the situation where 17.12% of all matter particles are baryonic ($\Omega_{\mathrm{B}} = 0.044$) and 82.88% are nonbaryonic dark matter.[1]

Often in *N*-body simulations, the number of particles is chosen to be the same as the number of cells in the domain grid, but in our simulations we have set the former (256^3) to be 8 times bigger than the latter (128^3). This choice obviously increases the mass resolution, but what is more important for us is that it produces a smoother and more reasonable dark-matter density on the grid. In order to see this, remember that only 82.88% of all particles are dark matter, which means that, if we use 128^3 rather than 256^3 particles, about $1/5$ of all the grid cells do not contain dark-matter particles at the initial time. The resulting

[1] It is time to stress that our $\Omega_{\mathrm{CDM}} = 8\pi G\rho_{\mathrm{CDM}}/3H_0^2$ is the fractional energy density of the bare dark-matter particles, which is *not* weighed by the coupling function $C(\varphi)$. As we mentioned in Appendix C and [20], $\rho_{\mathrm{CDM}} \propto a^{-3}$ as in ΛCDM but the behavior of $C(\varphi)\rho_{\mathrm{CDM}}$ (which is the actual quantity appearing in the Poisson equation) can be rather complicated. In all models we are simulating, including the ΛCDM one, we have the same ρ_{CDM}, *rather than* $C(\varphi)\rho_{\mathrm{CDM}}$, at present day.

dark-matter density therefore shows some artificial discreteness, which not only does not reflect reality but might also cause the solver for the scalar-field equation to diverge. By having more particles, we can make the dark-matter densities smoother and resolve the problem of overdiscreteness.[2]

C. Background and linear perturbation evolution

In general, a coupling between the scalar field and the dark-matter particles not only affects the force law and clustering properties of those particles [as described by Eqs. (14), (15), and (21)–(23)], but it also influences the background and linear perturbation evolution of the Universe. The modification in the background cosmic expansion rate directly changes the rate of the matter clustering, while the modification in the linear perturbation growth might lead to a different initial condition for the N-body simulation from the ΛCDM result. Consequently, we must take appropriate care of these issues in the N-body simulations in order to obtain reliable and complete numerical results.

The background expansion rate of the Universe is completely governed by (the zeroth order parts of) the scalar-field equation of motion

$$\ddot{\varphi} + 3H\dot{\varphi} + V_{\varphi} + C_{\varphi}\rho_{\rm CDM} = 0, \tag{31}$$

the Friedman equation

$$3H^2 = \kappa[\rho_{\rm B} + \rho_{\rm RAD} + C(\varphi)\rho_{\rm CDM} + \tfrac{1}{2}\dot{\varphi}^2 + V(\varphi)] \tag{32}$$

where $H = \dot{a}/a$ is the Hubble expansion rate and $\rho_{\rm RAD}$ includes contributions from photons and massless neutrinos (i.e., radiation), and the Raychaudhuri equation

$$3(\dot{H} + H^2) = -\frac{\kappa}{2}[\rho_{\rm B} + 2\rho_{\rm RAD} + C(\varphi)\rho_{\rm CDM} + 2\dot{\varphi}^2 - 2V(\varphi)]. \tag{33}$$

The introduction of Eq. (31) introduces a new degree of freedom φ to the system, for which the initial condition and relevant parameter [the Λ in $V(\varphi)$] should be chosen appropriately to guarantee consistency. More explicitly, we have to adjust the values of Λ and $\varphi_{\rm ini}$, $\dot{\varphi}_{\rm ini}$ so that today $H = H_0$ where H_0 is the measured Hubble constant which we set to be 71.9 km/s/Mpc in this work. This is a nontrivial requirement and is achieved through a trial-and-error process. We shall leave all the details of the numerical algorithm to Appendix C, as they are not our major concern here.

[2]Note that the higher-than-usual mass resolution is adopted only to ensure that the scalar-field solver converges. As we shall see below, the fifth force is shown to be proportional to gravity in our models, and agreement with analytical expectation shows that our choice works well. Once the fifth force is obtained, the remainder of the code is simply the default MLAPM and the mass resolution is high enough. Higher resolution is not needed for the scalar-field solver or the Poisson solver.

In Fig. 1 we have shown some representative results for the influences of the scalar-field coupling on the background cosmology. Clearly, for fixed α, increasing $|\gamma|$ means increasing the coupling strength, leading to more dramatic evolution of the scalar field, and this is why in the lower right panel we can see that as $|\gamma|$ increases, so the quantity $e^{\gamma\varphi}$ falls increasingly below 1. Meanwhile, as the scalar field rolls faster for larger $|\gamma|$, the equation of state parameter w approaches -1 (potential-energy-dominated regime) later in time (the upper right panel). Also, because $e^{\gamma\varphi}$ deviates more from 1, the contribution of the coupled dark matter ($\rho_{\rm cc} = \rho_{\rm CDM}e^{\gamma\varphi}$ in which $\rho_{\rm CDM} \propto a^{-3}$, see Appendix C) to the Friedmann equation [Eq. (32)] is smaller and the contributions from other matter species are greater (upper left panel). Because dark matter is the principal ingredient driving the expansion of the Universe in the matter-dominated era, this in turn implies that the expansion rate will differ from the ΛCDM prediction (lower left panel). Note that the change of expansion rate at early times necessarily cause the matter power spectrum at $z \sim 50$ to differ from the ΛCDM result, a point we will return to shortly.

In Fig. 2 we have displayed the effects of the scalar-field coupling on the linear cosmic microwave background (CMB) and matter power spectra. Because of the decrease in the expansion rate, the angular diameter distance increases so that the peaks of the CMB spectrum are shifted rightwards, and on large scales the perturbation in the scalar field (cf. Fig. 4 below) modifies the integrated Sachs-Wolfe effect to increase the power at low ℓ. The matter power spectrum, on the other hand, is increased on all scales: on large scales this is purely because the Universe is now expanding more slowly, allowing matter to cluster more. On small scales there is another effect—the boost due to the scalar-field fifth force, which is almost always proportional to gravity in magnitude and parallel in direction (see below). It is clear from the figure that the results are rather insensitive to the parameter α, and so in what follows we shall only consider the case of $\alpha = 0.1$.

Since we need to know the matter power spectrum at early time $z \sim 50$ in order to generalize initial conditions for the N-body simulations, we also plot it in Fig. 3. We further separate the baryons from dark matter, the latter being our major concern: on small scales it is clear that the dark-matter power spectrum is greater than that of baryons, due to the extra fifth force it experiences (cf. upper panels). Most interestingly, we see that even at $z = 49$ the dark-matter power spectra for different models can be rather different, again due to the modified expansion rate and the fifth force. This means that in our N-body simulations we should *not* use the same initial condition (as in [20,22], where the chameleon effect is so strong that at early times the matter power spectrum is indistinguishable from that of ΛCDM). Instead, we should generate initial conditions separately for different models (in our case different values for γ)—this is the topic of Sec. III D and Appendix A.

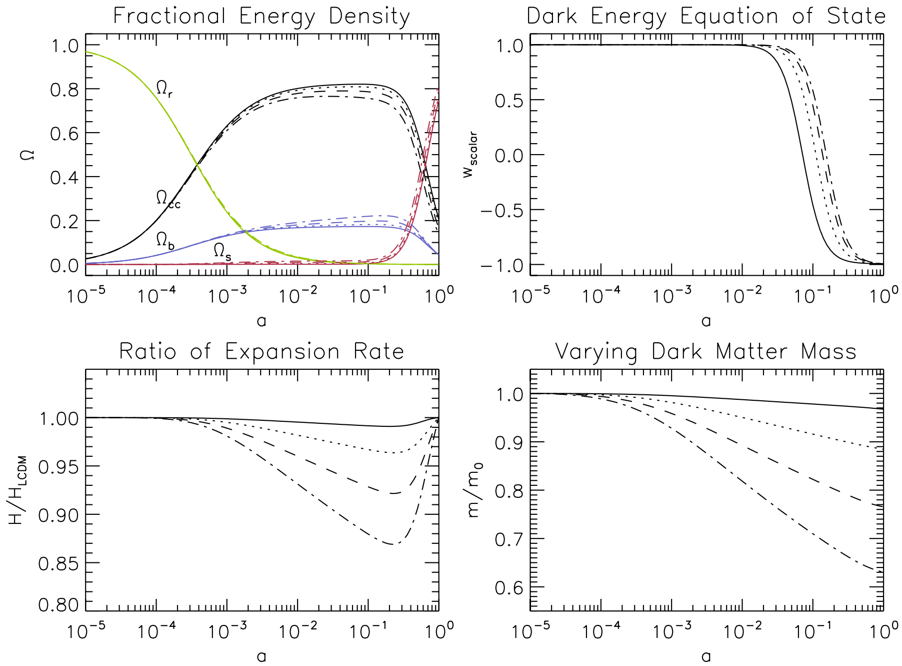

FIG. 1 (color online). Figures to illustrate the background evolution of our coupled-scalar-field models. Upper left panel: The fractional energy densities for radiation (green), *coupled* dark matter (black), baryons (blue), and the scalar field (red), as denoted by the notations beside the corresponding cures; note that $\Omega_{\rm cc} = 8\pi GC(\varphi)\rho_{\rm CDM}/3H^2$. Upper right panel: The equation of state of the scalar field, $w \equiv p_\varphi/\rho_\varphi$ in which $p_\varphi = \frac{1}{2}\dot{\varphi}^2 - V(\varphi)$ and $\rho_\varphi = \frac{1}{2}\dot{\varphi}^2 + V(\varphi)$. Lower left panel: The ratio between the Hubble expansion rate in the coupled-scalar-field model and that in the ΛCDM paradigm, other physical parameters such as $\rho_{\rm B}$, $\rho_{\rm RAD}$, $\rho_{\rm CDM}$ being held the same, as a function of the scale factor a. Lower right panel: The "varying mass" of the dark-matter particles as a function of a—here m_0 is the *constant bare* mass of the particles and $m = e^{\gamma\varphi}m_0$. In all figures we have chosen $\alpha = 0.1$ and the solid, dotted, dashed, and dot-dashed curves represent the models with $\gamma = -0.05$, -0.10, -0.15, and -0.20, respectively.

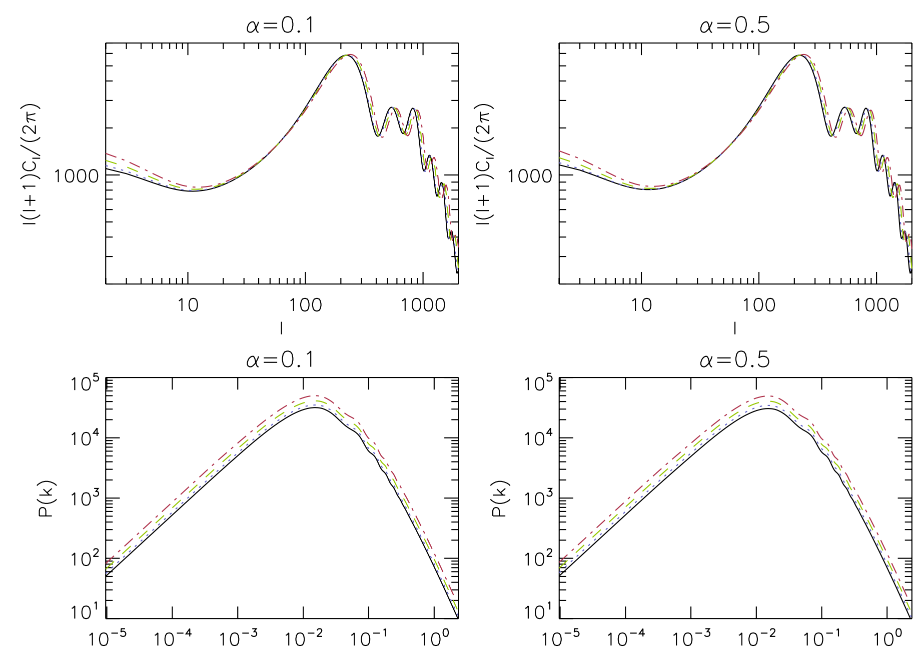

FIG. 2 (color online). The linear power spectra of the coupled-scalar-field model. Upper left panel: The cosmic microwave background (CMB) power spectra for the four models with $\alpha = 0.1$. Upper right panel: The same but for the models with $\alpha = 0.5$. Lower left panel: The matter power spectra at present day (redshift $z = 0$) for the four models with $\alpha = 0.1$. Lower right panel: The same but for the models with $\alpha = 0.5$. In all figures the solid (black), dotted (blue), dashed (green), and dot-dashed (red) curves represent the models with $\gamma = -0.05$, -0.10, -0.15, and -0.20, respectively.

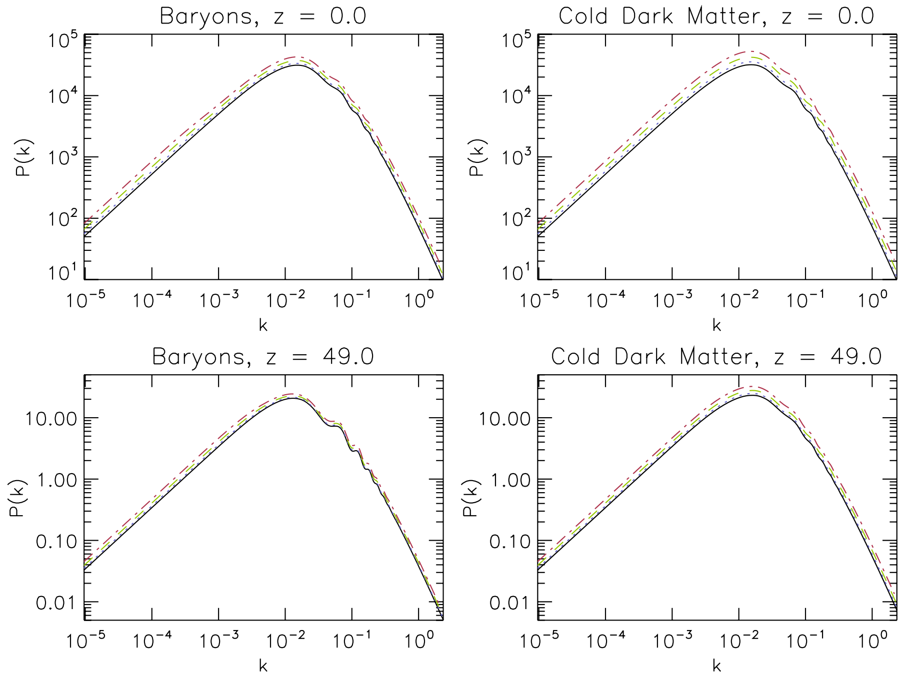

FIG. 3 (color online). Upper panels: The matter power spectra for baryons only (left) and for dark matter only (right), at current time ($z = 0$). Lower panels: The same but at an earlier time $z = 49$ where the initial condition for the N-body simulations are computed. In all figures $\alpha = 0.1$ and the solid (black), dotted (blue), dashed (green), and dot-dashed (red) curves represent the models with $\gamma = -0.05$, -0.10, -0.15, and -0.20, respectively.

D. Initial conditions for the N-body code

As we described in detail above, the fact that the scalar-field-dark-matter coupling begins to take effect at rather high redshift indicates that the initial conditions for the N-body simulations of our coupled-scalar-field models (at redshift $z_i \sim 50$ here) will also be different from those in ΛCDM. To account for this modification, the most straightforward approach is to generate the linear matter power spectra for our coupled-scalar-field models at the starting redshift $z_i \sim 50$, and utilize them to produce the Gaussian random density fluctuation field and displace the particles. In GRAFIC2 the matter power spectrum is generated at time $z = 0$, normalized to a preselected value and then evolved back to z_i and used to displace particles. We shall not follow this in our work; instead we adopt the same initial condition in CAMB at redshift $z \sim 10^6$ for all models including the ΛCDM one and evaluate the power spectrum at z_i—in this way the linear σ_8 today will be different for different models (in contrast σ_8 is the same for all models in some other works). This is because we are interested in how the scalar field affects the evolution of structure as compared to ΛCDM, given the same initial condition at very early times.

In principle, the matter power spectrum at z_i that is used in GRAFIC2 needs to be generated for each model, for example, by linear perturbation code that is the default in GRAFIC2; however, here we adopt a more economical method. To see this, in the upper panels of Fig. 4 we have displayed the time evolution of $[D_+ - D_{+,\Lambda\mathrm{CDM}}]/D_{+,\Lambda\mathrm{CDM}}$ as well as $[\dot{D}_+ - \dot{D}_{+,\Lambda\mathrm{CDM}}]/\dot{D}_{+,\Lambda\mathrm{CDM}}$, with D_+ being the linear growth factor we have discussed in Appendix D. For simplicity, we only show these for the two models with $\alpha = 0.1$ and $\gamma = -0.05$, -0.15 as indicated in the figure, and for each model the solid, dotted, dashed, and dash-dotted curves represent, respectively, the results for $k = 0.0001$, 0.001, 0.01, and 0.1 Mpc^{-1}. There are several important features in these plots. First, at early times ($z \gtrsim 10^4$) we see that the difference is negligible as the scalar field has yet to take effect. Second, on large scales (small k) the results tend to converge to a curve which describes how the change of background expansion rate modifies the density growth (the fifth force has no effect here because the scale is out of its range). Third, on smaller scales (large k) the fifth force begins to act and further enhances the growth of dark-matter density perturbation. These plots show that $\tilde{D}_+$, the dark-matter linear growth factor, depends on both k and time, as we mentioned in Appendix D, and this must be taken into account.

As detailed in Appendix D, the displacement and peculiar velocity of particles are given by $D_+\mathbf{d}$ and $\dot{D}_+\mathbf{d}$, respectively, where $\mathbf{d}$ is a vector which is the same for different models (remember, again, we start with the same initial condition in CAMB at $z \sim 10^6$). Consequently, the differences in the displacements and peculiar velocities in our models are equivalent to the differences in $D_+(z_i)$ and $\dot{D}_+(z_i)$. Instead of evaluating $D_+(z_i)$ and $\dot{D}_+(z_i)$ with (a modified version of) GRAFIC2 for each model, we use the ΛCDM results for $D_+(z_i)$ and $\dot{D}_+(z_i)$ computed by

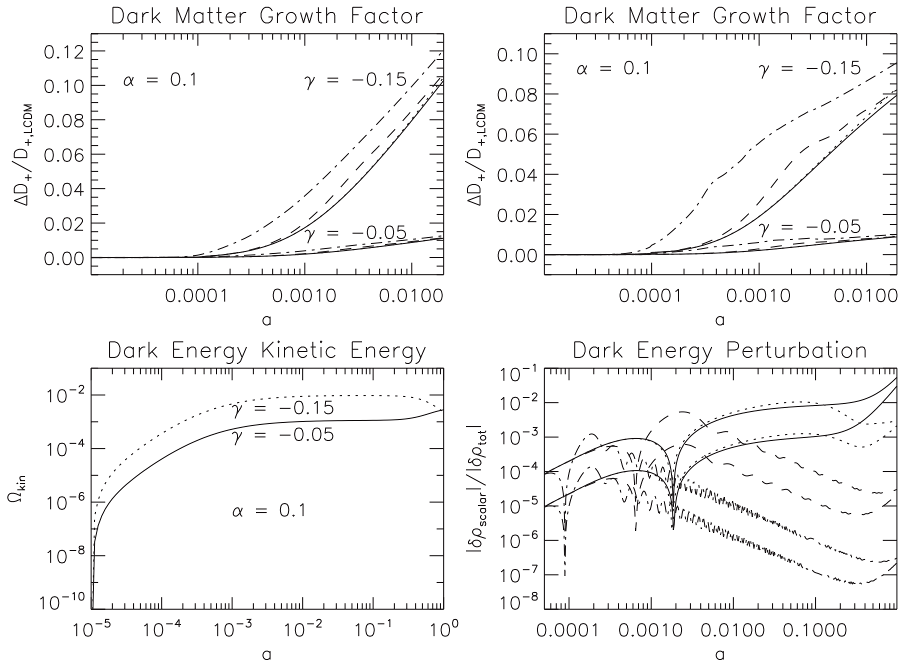

FIG. 4. Upper left panel: The fractional change of the growth factor D_+ of the dark-matter density perturbation in the coupled-scalar-field model as compared with the ΛCDM prediction; for clearness, only the results for the two models with $\alpha = 0.1$, $\gamma = -0.05$ and $\alpha = 0.1$, $\gamma = -0.15$ are shown, as indicated above the curves, and for each model the solid, dotted, dashed, and dot-dashed curves represent, respectively, the result for $k = 0.0001$, 0.001, 0.01, and 0.1 Mpc^{-1}. Upper right panel: The same as above, but for the fractional change of $\dot{D}_+$ as a function of the scalar factor a. Lower left panel: The time evolution of the fractional energy density of the *kinetic energy* of the scalar field, $\Omega_{\mathrm{kin}} = 4\pi G\dot{\varphi}^2/3H^2$ for the two models with $\alpha = 0.1$, $\gamma = 0.05$ (solid curve) and $\alpha = 0.1$, $\gamma = -0.15$ (dotted curve), respectively. Lower right panel: The evolution of the density contrast of the scalar field, of which the energy density is $\rho_\varphi = \frac{1}{2}\dot{\varphi}^2 + V(\varphi)$; the solid, dotted, dashed, and dot-dashed curves are for four different length scales $k = 0.0001$, 0.001, 0.01, and 0.1 Mpc^{-1}, respectively, and for each style of curve the upper (lower) one is for the model with $\alpha = 0.1$, $\gamma = -0.15$ ($\alpha = 0.1$, $\gamma = -0.05$).

GRAFIC2, and also calculate $\mu_1 \equiv D_+/D_{+,\Lambda\mathrm{CDM}}$ and $\mu_2 \equiv \dot{D}_+/\dot{D}_{+,\Lambda\mathrm{CDM}}$ at z_i using CAMB. Then the particle displacement and peculiar velocity in the coupled-scalar-field models are simply given, respectively, by $\mu_{1,2}$ times those generated by GRAFIC2.

Furthermore, we shall take into account the differences between the coupling and noncoupling matter species as follows. The baryons do not feel the fifth force (remember that "baryons" here simply means noncoupling dark-matter particles, and this is why we do not use the baryon matter power spectrum generated by CAMB to displace these particles). The difference between the baryonic linear growth factor D_+ from $D_{+,\Lambda\mathrm{CDM}}$ is mainly due to the modified expansion rate,[3] and so we use the D_+ calculated for very small k to evaluate $\mu_{1,2}$ for baryons. Dark-matter particles, on the other hand, do feel the fifth force which, on small scales, has a magnitude of $2\gamma^2$ times that of gravity, and so we use the $\tilde{D}_+$ calculated for large k to evaluate $\tilde{\mu}_{1,2}$ for dark matter. In this way, the bias between the two matter species is approximately reflected in our initial conditions. The scale dependence of D_+ does not appear to have been considered in generating initial conditions in the earlier literature.

When generating the initial displacement and peculiar velocities of particles, we run a random number generator for a variable with a uniform distribution $U[0, 1]$. As mentioned above, if the number generated is less than $\Omega_\mathrm{B}/(\Omega_\mathrm{B} + \Omega_{\mathrm{CDM}})$, we tag the particle as a baryon and use $\mu_{1,2}$ to displace it; otherwise we tag the particle as dark matter and use $\tilde{\mu}_{1,2}$ to compute its displacement and velocity. Once this has been done, no particle will ever be retagged so that the consistency is not spoiled. Those particles tagged as dark matter will contribute to the scalar-field evolution and be influenced by the scalar-field fifth force, while those which are tagged as baryons will not.

IV. SIMULATION RESULTS

In this section we present the main results from the *N*-body simulations we have performed. We start by listing some preliminary results to give a rough idea about the effects of the couplings we are studying.

[3]The baryonic growth factor is also affected by the fact that dark matter, clustering more strongly than in ΛCDM, can produce a deeper potential, which attracts baryons more strongly. However, the main factor affecting the baryonic linear growth factor is still the modified background expansion rate [43].

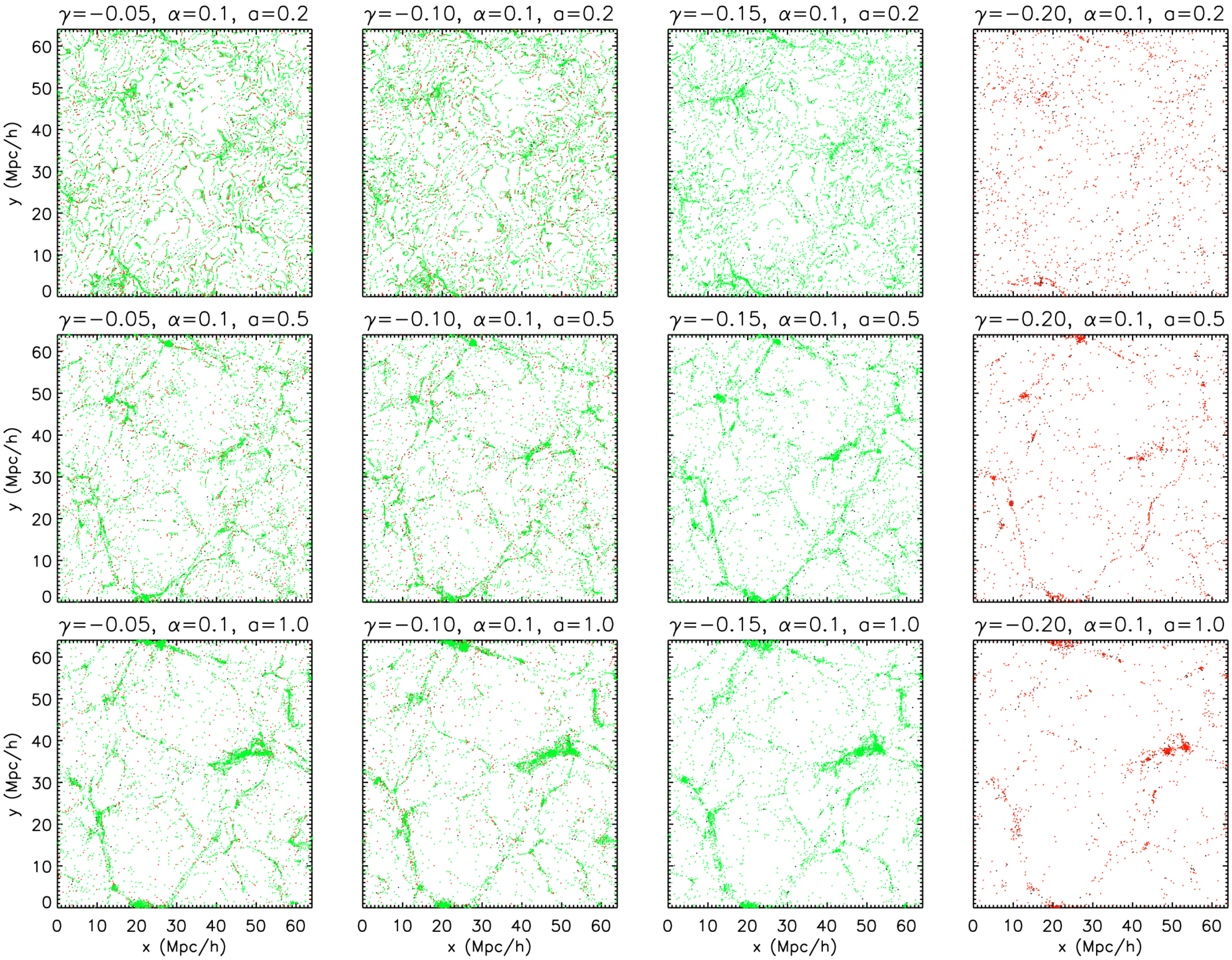

FIG. 5 (color online). Snapshots of the particle distribution in our four coupled-scalar-field models as indicated by the subtitles of the panels. a is the scale factor and $a = 1$ is the present time. For clearness, we only pick out a slice of the simulation box with $30h^{-1}$ Mpc $< z < 30.3h^{-1}$ Mpc and $0h^{-1}$ Mpc $< x, y < 64h^{-1}$ Mpc. The green dots represent dark-matter particles and red dots baryons. Note that in the third column we have plotted only dark matter and in the fourth column only baryons, to produce better visual distinction between the two.

A. Preliminary results

In Fig. 5 we show snapshots of the particle distribution at different output times. We can see clearly the trend of matter clustering. The blue and red dots are the dark-matter and baryons particles, respectively.

Since one of the most important influences of the scalar-field coupling is to exert a fifth force on the dark-matter particles, we are interested in the magnitude of the fifth force as compared with that of gravity. This is given in Fig. 6, where we have again displayed the results for the simulated models at different output times. To understand this figure, note that if the contributions from the scalar-field potential to the Poisson equation and scalar-field equation of motion are negligible (which turns out to be the case in our simulations) and if all particles (dark matter and baryons) have the same coupling to the scalar field, then the right-hand sides of Eqs. (28) and (29) are proportional, with a coefficient 2γ, which implies that $u = 2\gamma\Phi_c$; thus Eq. (27) says that the strengths of fifth force (f) and gravity (g) should satisfy $f = 2\gamma^2 g$.

In our models only a fraction $\Omega_{\rm CDM}/\Omega_m$, where $\Omega_m = \Omega_{\rm CDM} + \Omega_{\rm B}$, of all the particles are coupled to the scalar field. Thus, assuming dark matter and baryonic particles are distributed in the same way, we should have

$$f = 2\gamma^2 \frac{\Omega_{\rm CDM}}{\Omega_m} g \tag{34}$$

because only a fraction $\Omega_{\rm CDM}/\Omega_m$ of the particles which produce gravity also produce the fifth force. Equation (34) is plotted in Fig. 6 as the solid lines. The dots are the simulation results for f/g for the particles outputted in

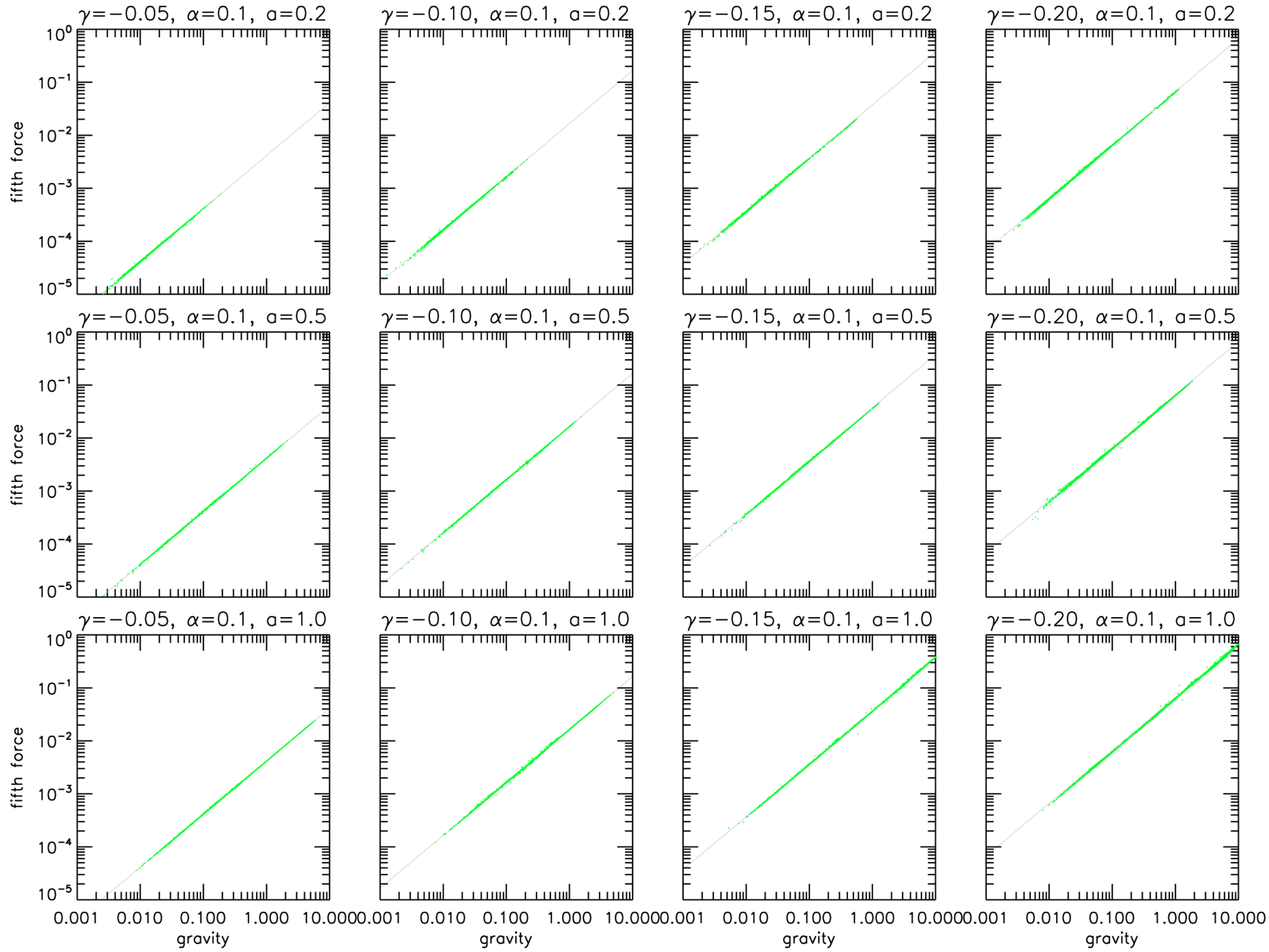

FIG. 6 (color online). The relation between the magnitudes of the fifth force and that of gravity for the four coupled-scalar-field models at three different output times $a = 0.2, 0.5, 1.0$. The black solid line in each panel represents the analytical approximation $f = 2\gamma^2 \cdot \frac{\Omega_{\rm CDM}}{\Omega_m} g$ (see text) and the ~150 000 dots (green) the results from the simulations. The particles are the same as those in Fig. 5.

Fig. 5. The agreement between the analytical approximation and numerical solution is remarkably good, which serves as a test of our Newton-Gauss-Seidel solver of the scalar-field equation of motion.[4]

Furthermore, Fig. 6 also shows some clearly different features from the results of [22], in which the fifth force is suppressed by the chameleon mechanism in certain cases (such as at early times and in high-density regions). Here, the fifth force is not suppressed because the potential $V(\varphi)$ is negligible, and the approximation Eq. (34) works well *anywhere* all the *time*. This confirms our earlier claim that the matter power spectrum will be changed at early times as will be the initial condition for the N-body code.

As should be evident now, the spatial configuration of the scalar field φ, or equivalently the rescaled scalar field u, should closely follow that of the gravitational potential Φ_c, for the same reasons that led to Eq. (34). Figures 7 and 8 confirm this: as can be seen there, for all the models and all the output times, the configurations of $-u$[5] and Φ_c are indistinguishable.

The above figures show that in our coupled-scalar-field models the fifth force f (scalar field u) closely mimics the gravity g (gravitational potential Φ_c), and so the approximation $f = 2\gamma^2 g$, used in many other previous simulation works (e.g., [30]), is a good one.

[4] Remember that the Poisson equation on either the domain grid or the refinement is solved using different methods from those for the scalar-field equation of motion.

[5] Note that we expect that $u = 2\gamma\Phi_c$ approximately as explained above, and $\gamma < 0$: the minus sign here ensures that Fig. 8 follows Fig. 7, rather than compensating it, so that we have a better visual impression.

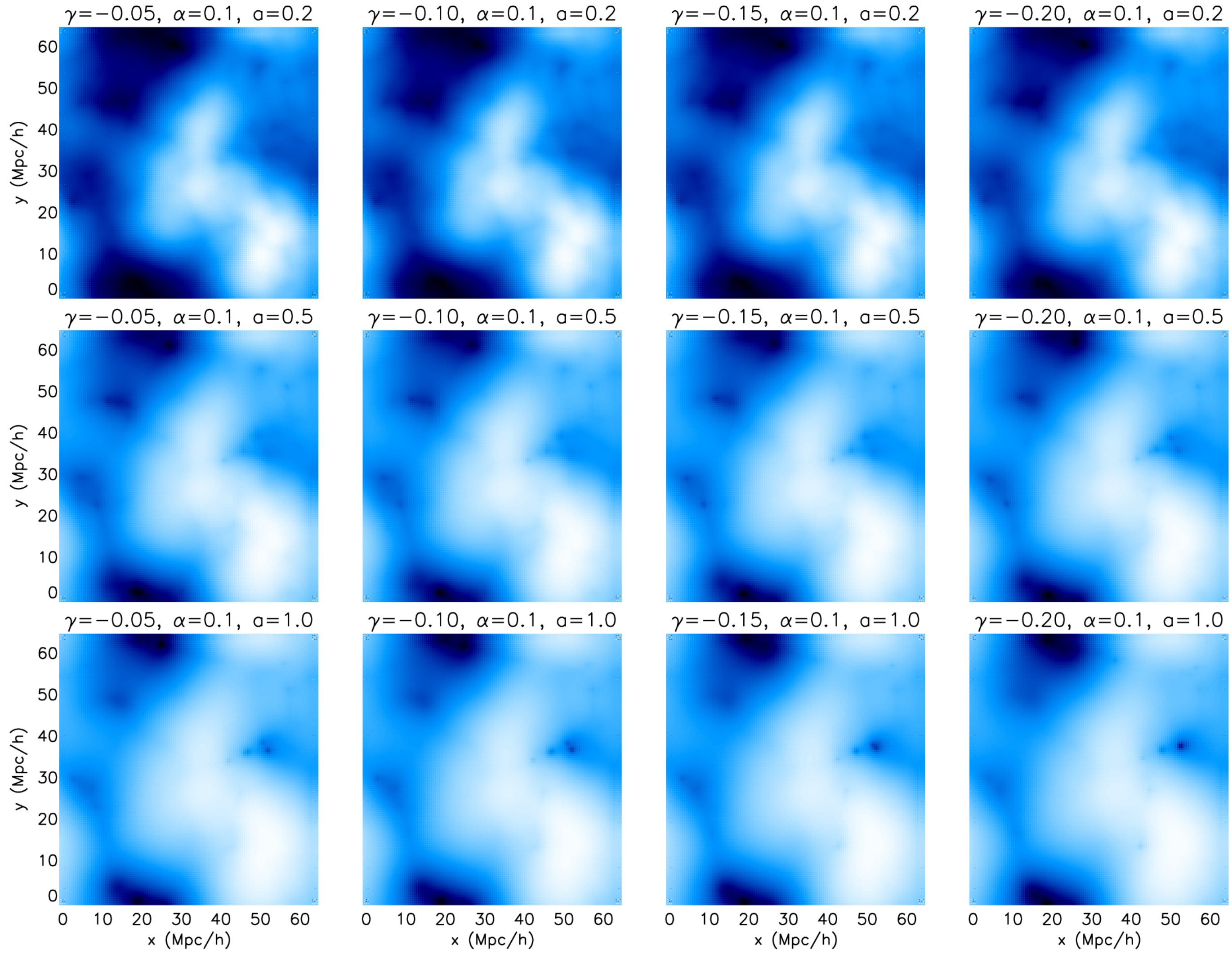

FIG. 7 (color online). The gravitational potential on the z plane where $z = 32h^{-1}$ Mpc. Dark regions are where the potential is deeper while light regions are where it is shallower. The four columns are for the four models we consider and the three rows are for three output times, respectively, $a = 0.2$, 0.5, and 1 where a is the cosmic scale factor.

B. Matter power spectrum

The nonlinear matter power spectrum measured from the output particle distribution is of more observational interest and it is the theme of this subsection. The matter power spectrum in the present work is measured using POWMES [44], which is a publicly available code based on the Taylor expansion of trigonometric functions and yields Fourier modes from a number of fast Fourier transforms controlled by the order of the expansion.

Figure 9 displays the fractional changes of the matter power spectra $P(k)$ due to the scalar field coupling, where $\Delta P \equiv P_{\mathrm{scalar}} - P_{\Lambda\mathrm{CDM}}$. For comparison, we have also shown the linear results as dashed curves. We can see that on large scales (small k) there is an overall agreement between the linear and nonlinear predictions, which is not surprising since those scales have not experiences much nonlinear complication. The agreement is very good at early times (the top panels) when nonlinear effects generally have not taken place on scales $k \sim 0.1h\ \mathrm{Mpc}^{-1}$; at late times (top curves in bottom panels) there is a slight mismatch, which is understandable because our simulation box is not big enough to allow measurement of $P(k)$ below $k = 0.1h\ \mathrm{Mpc}^{-1}$ where nonlinear effects already enter. Indeed, even in the latter case, we can see the trend that the linear and nonlinear curves merge towards small k. The fact that the nonlinear $P(k)$ reduces to the linear one on large scales is not trivial as the background cosmology in our N-body simulations has also been modified[6] (as it is in CAMB, which is used for the linear calculation), and we take this as another test of our modified MLAPM code.

[6]As mentioned above: the larger $|\gamma|$, the slower the Universe expands (cf. Fig. 1, lower left panel), and thus the more growth the matter perturbations experience and the larger $P(k)$ becomes.

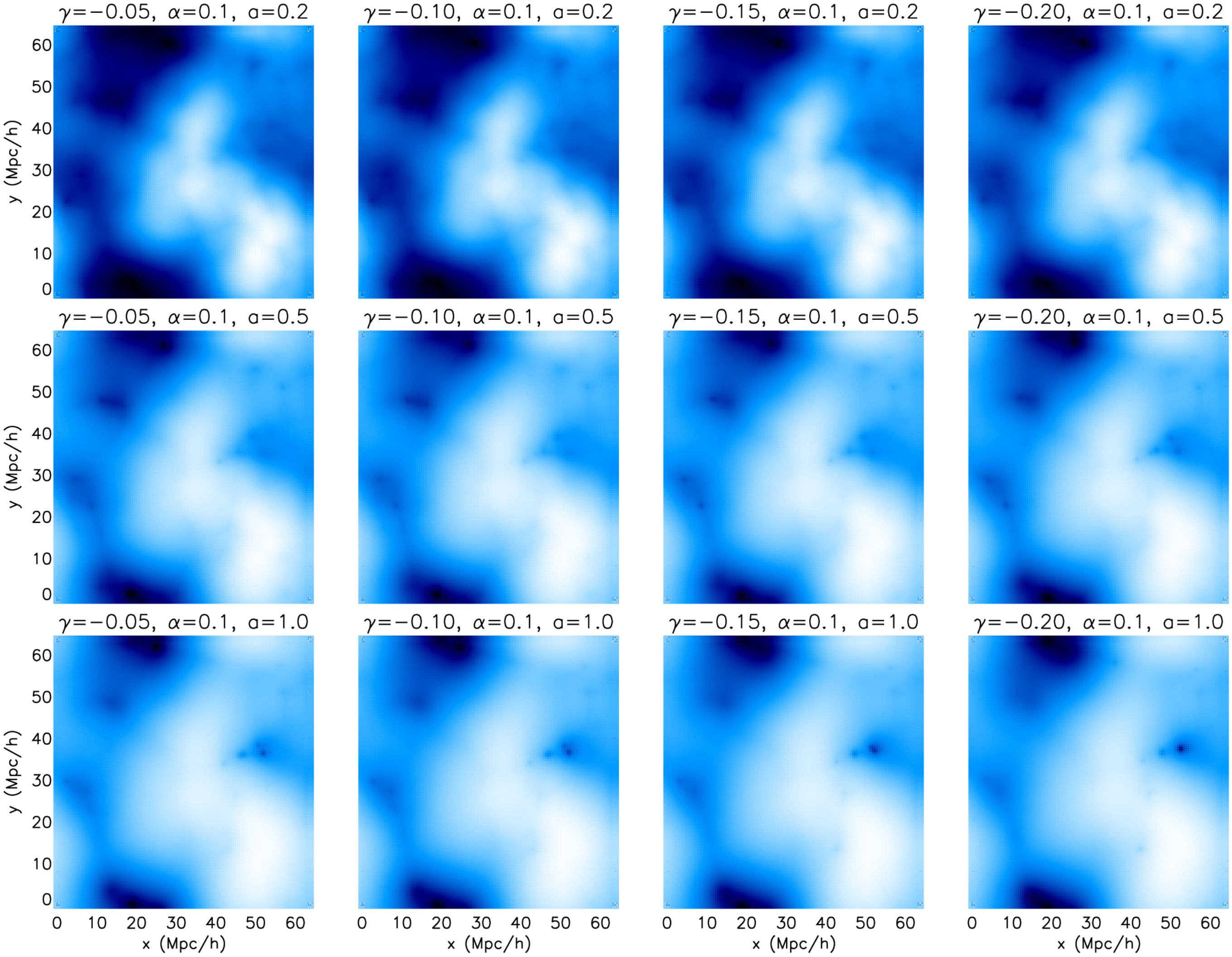

FIG. 8 (color online). The same as Fig. 7 but for $-\varphi$ where φ is the value of the scalar field. The negative sign is added to make the plot look similar to Fig. 7, and otherwise they will be compensating for each other.

The main advantage of the N-body simulation is its ability to probe the nonlinear structure formation and so we are more concerned with the $P(k)$ on smaller scales, which is also plotted in Fig. 9. We can see that on intermediate scales ($k \sim 1h$ Mpc^{-1}) the nonlinear $P(k)$ beats the linear one, but on even smaller scales it falls behind the linear value again. For the four models in our simulations, the enhancements of the matter power range from negligible to $\sim$100%, but much of the enhancement is due to the modified background expansion and is already seen in the linear results.

More interestingly, the enhancement is more significant at earlier times. This can been understood as follows: at later times the contribution of the dark-matter density to the Poisson equation (and thus the gravitational potential) is decreased due to the coupling function $C(\varphi)$ becoming increasingly less than 1, weakening further clustering of the dark and the baryonic matter. Note that such a trend can also be seen in the linear $P(k)$, by comparing the bottom panels, although it is not so obvious. The strong enhancement of the matter power spectrum at early times (notably $z \sim 2$–4, as can be seen and inferred from our linear and nonlinear plots), means that Ly-α flux might be a good test bed for the coupled-scalar-field models, as has been investigated recently in [45]. Also, the big differences between the matter power spectra for coupled-scalar-field and ΛCDM models show that the Sloan Digital Sky Survey data could place stringent constraints on the model parameters. However, one must be careful to note that what we have obtained is only the dark-matter power, rather than the galaxy spectrum, and there is a bias between the two which can only be computed by including real baryons in the simulations, which is beyond the scope of the current work. Weak gravitational lensing, for example, is sensitive to the magnitude of matter perturbations and thus could be a cleaner test of our models.

In order to display the bias developed between baryons and dark matter, we have also plotted the $P(k)$ for baryons

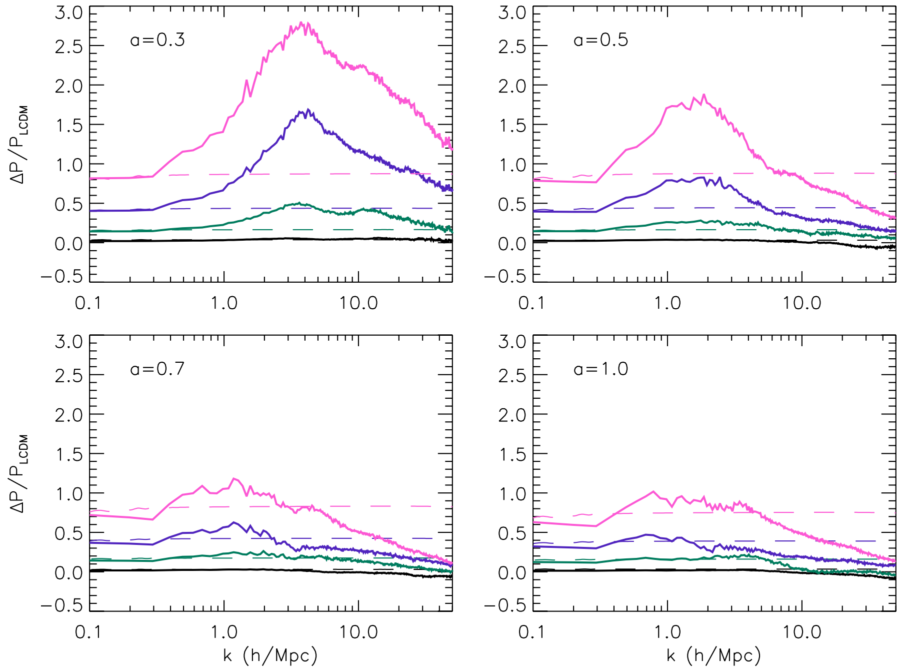

FIG. 9 (color online). The linear and nonlinear matter power spectra $P(k)$ as compared with those of the ΛCDM paradigm. Shown are the fractional change of $P(k)$ for the four models with $\alpha = 0.1$ (from bottom to top on the left-hand side) and $\gamma = -0.05$ (black curves), -0.10 (green), -0.15 (blue), -0.20 (purple), and at four different output times $a = 0.3$ (upper left panel), 0.5 (upper right), 0.7 (lower left), 1.0 (lower right). Solid curves are from N-body simulations and dashed curves from linear perturbation calculation.

and dark matter separately in Fig. 10. As expected, the $P(k)$ for dark matter is always larger, signifying a stronger clustering due to the assistance from the fifth force. The larger $|\gamma|$ is, the stronger the fifth force will be, and the larger the bias will become.

C. Mass function

We identify halos in our N-body simulations using MHF (MLAPM halo finder) [46], which is the default halo finder for MLAPM. MHF utilizes the refinement structure of the MLAPM grids to pin down the regions where potential halos are and organize the refinement hierarchy into a tree structure. MLAPM refines grids according to the particle density on them, and so the boundaries of the refinements are simply isodensity contours. MHF collects the particles within these isodensity contours (as well as some particles outside), and performs the following operations: (i) assuming spherical symmetry of the halo, calculates the escape velocity $v_{\rm esc}$ at the position of each particle, and (ii) removes the particles whose velocities exceed $v_{\rm esc}$. Steps (i) and (ii) are then iterated until all unbound particles are removed from the halo, or the number of particles in the halo falls below a predefined threshold, which is 20 in our simulations. Note that the removal of unbound particles is not present in some halo finders that use the spherical overdensity (SO) algorithm, which includes the particles in the halo as long as they are within the radius of a virial density contrast, regardless of whether they are too fast to be confined in the halo.

As explained in detail in [22], part of the MHF algorithm also needs to be modified for the coupled-scalar-field model, because the scalar field φ behaves as an extra "potential" (which produces the fifth force) and so the dark-matter particles experience a deeper total "gravitational" potential than in the ΛCDM paradigm, all other things being equal. Consequently, the escape velocity for dark-matter particles increases compared with the Newtonian prediction.

In the models we are considering here, things are even more complicated. In [22], the chameleon mechanism ensures that the scalar field takes a very tiny value everywhere, all the time (typically $\sqrt{\kappa}\varphi \lesssim 10^{-5}$) and so the coupling function $C(\varphi) = e^{\gamma\sqrt{\kappa}\varphi} \doteq 1$ is a very good approximation—this means that the contribution of the dark matter to the Poisson equation is not significantly modified compared with that in ΛCDM. In the models here, however, $C(\varphi)$ can be up to 30% less than 1, so that the source term of the Poisson equation is significantly different from ΛCDM.

Obviously, we need to take both of these two major changes into account when we design a new algorithm to identify halos.

The default MHF code works out $v_{\rm esc}$ using the Newtonian result

$$v_{\rm esc}^2 = 2|\Phi|, \tag{35}$$

in which Φ is the gravitational potential. Under the assumption of *spherical symmetry* for the halos, the

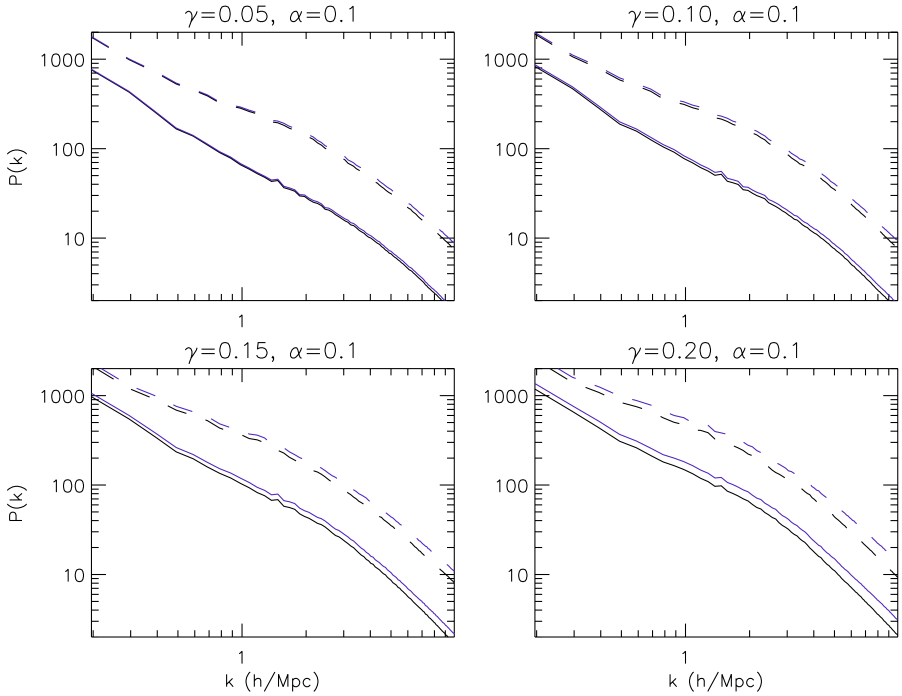

FIG. 10 (color online). The bias between the nonlinear matter power spectra $P(k)$ of dark matter and baryons for the four models we are simulating, as indicated in the subtitles of the panels. The solid curves are for the output time $a = 0.5$ and dashed curves for $a = 1.0$. For each style of curve the lower (black) one is for baryons and the upper (purple) one is for dark matter.

Poisson equation $\nabla^2\Phi = 4\pi G\rho_m$ could be integrated once to give

$$\frac{d\Phi}{dr} = \frac{GM(<r)}{r^2} \tag{36}$$

which is just the Newtonian force law. This equation can be integrated once again to obtain

$$\Phi(r) = G\int_0^r \frac{M(<r')}{r'^2}dr' + \Phi_0 \tag{37}$$

where Φ_0 is an integration constant and can be fixed [47] by requiring that $\Phi(r = \infty) = 0$ as

$$\Phi_0 = \frac{GM_{\mathrm{vir}}}{R_{\mathrm{vir}}} + G\int_0^{R_{\mathrm{vir}}} \frac{M(<r')}{r'^2}dr', \tag{38}$$

in which R_{vir} is the virial radius of the halo and M_{vir} is the mass enclosed in R_{vir}.

In the coupled-scalar-field models here, the two modifications mentioned above are reflected in Eqs. (35) and (36) .

For Eq. (35), we realize that the gravitational potential Φ is not the only factor determining the escape velocity: there is also a contribution from the scalar field φ. When the fifth force is added, we call its contribution to the total gravitational potential Φ_φ and its value at infinity now no longer Eq. (35), but given by

$$v_{\mathrm{esc}}^2 = 2|\Phi + \Phi_\varphi - \Phi_0 - \Phi_{\varphi 0}|. \tag{39}$$

We have recorded the components of gravity and the fifth force for each particle in the simulation, and so the ratio f/g can be computed at the position of each particle, which gives $(\Phi_\varphi - \Phi_{\varphi 0})/(\Phi - \Phi_0)$ at that position, which can be used in Eq. (39). In this way we have, at least approximately, taken into account the fifth force and Φ_φ. (We find that the mass function measured using our modified algorithm deviates by a few percent from that measured using the SO method.)

For Eq. (36), which is used to compute Φ and Φ_0, we know that it is applicable in the coupled-scalar-field model as well, because the contribution from the scalar-field potential is negligible. But one should be careful when interpreting the mass M here: it is *not* the total bare mass of all the particles ($M_{\mathrm{B}} + M_{\mathrm{CDM}}$) within radius r, but $M_{\mathrm{B}} + C(\varphi)M_{\mathrm{CDM}}$. Such a fact can be taken into account by multiplying the mass of each *dark-matter* (not baryonic) particle by $C(\varphi)$, which is evaluated using the φ at the position of that particle (which we have recorded too). Note that observations of the masses are made by registering gravitational effect, and so the halo mass we measure should be $M_{\mathrm{B}} + C(\varphi)M_{\mathrm{CDM}}$ rather than $M_{\mathrm{B}} + M_{\mathrm{CDM}}$: in what follows we will always talk about the former unless otherwise stated.

In Fig. 11 we have plotted the mass functions of our four coupled-scalar-field models at the current time, as compared with the prediction of the ΛCDM paradigm. Obviously, as the coupling between dark matter and the scalar field becomes stronger, more heavy halos will be

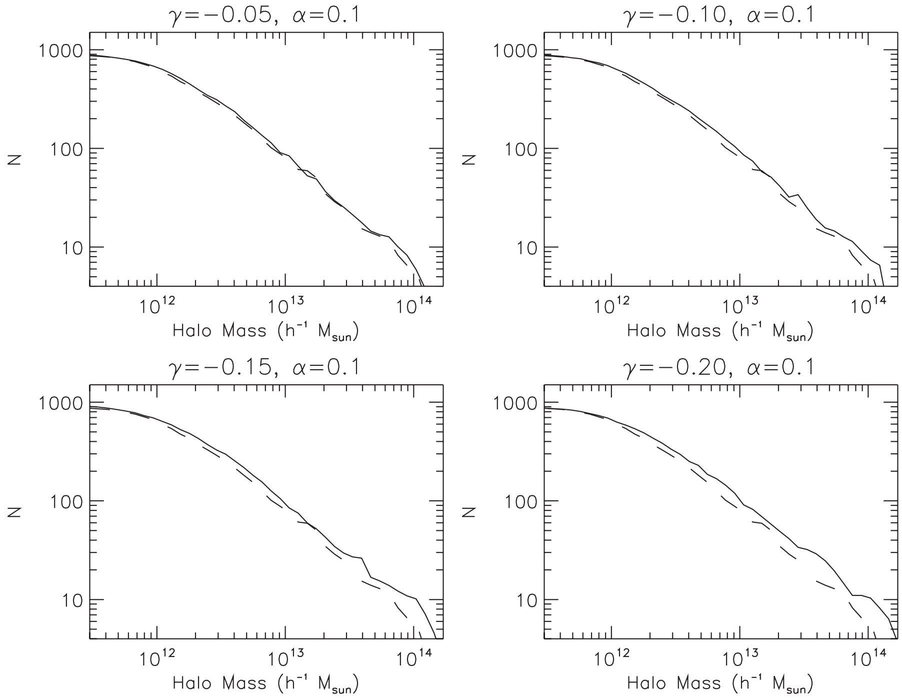

FIG. 11. The mass functions at $a = 1$ for the four coupled-scalar-field models under investigation, as indicated by the subtitles of the panels. The dashed curves are the corresponding result of ΛCDM.

produced during structure formation. However, it is not yet clear which physical effect is mainly responsible for such a pattern, and several factors could be crucial. For examples, as $|\gamma|$ increases, the fifth force strengthens and the background expansion gets slower, both of which would help boost the clustering of matter; on the other hand, the dark-matter's contribution to the Poisson equation is weakened due to $C(\varphi)$ becoming increasingly less than 1—this will weaken the clustering of matter. Detailed study of the significance of these different physical effects is beyond the scope of this work, and will be given in [43].

Before closing this section, however, we emphasize that halo identification is a complicated issue, and there is no unambiguously best algorithm to do it. Certain other algorithms, such as the SO, friend-of-friend, and those based on Voronoi tessellation, are also popular choices. However, even if other methods are used, it is also important to bear in mind that the coupled-scalar-field effect should be taken into account when searching for halos, in one way or another.

D. Halo properties

Finally, we are also interested in the properties of the dark-matter halos in the coupled-scalar-field models. In the case of a chameleonlike scalar field, Ref. [22] shows that there is a strong environmental dependence on density profile and baryon-dark-matter bias inside the halo, which is controlled by the model parameters in a complicated way. In the models generated here, the fifth force is everywhere unsuppressed and we do not expect such an environmental dependence as seen in [22]. However, we have several factors mentioned in Sec. IV C, which can potentially lead to interesting new features.

We will look first at the internal density profiles, which can be measured down to small radii thanks to the higher spatial resolution of the self-refinement code. We have selected two typical halos from each simulation. Halo I is centered on $(x, y, z) \sim (32.4, 31.5, 61.2)h^{-1}$ Mpc, which is slightly different for different simulations, and has a virial mass $M_{\rm vir} \sim 1.29 \times 10^{14} h^{-1} M_\odot$; halo II is centered on $(x, y, z) \sim (54.8, 39.8, 35.7)h^{-1}$ Mpc, which is also slightly different for different simulations, and has a virial mass $M_{\rm vir} \sim 1.90 \times 10^{13} h^{-1} M_\odot$ (note here that the virial masses are for the ΛCDM *simulations*; for scalar-field simulations they can be, and generally are, larger).

Figure 12 summarizes the results, and shows that the density profile for the coupled-scalar-field model is rather similar to that of ΛCDM, except that in the innermost part, the overdensity for the scalar-field model (solid curves) drops below that of ΛCDM (dashed curves). Such a phenomenon has previously been detected by the authors of [31] and explained as mainly due to the velocity-dependent acceleration of dark-matter particles [the last term in Eq. (19)]. However, here we find that such a trend does *not* continue with increasing $|\gamma|$ and indeed is reversed for large $|\gamma|$ values.

In the ΛCDM paradigm, it is well known that the internal density profiles of dark-matter halos are very well described by the Navarro-Frenk-White (NFW) [48] profile

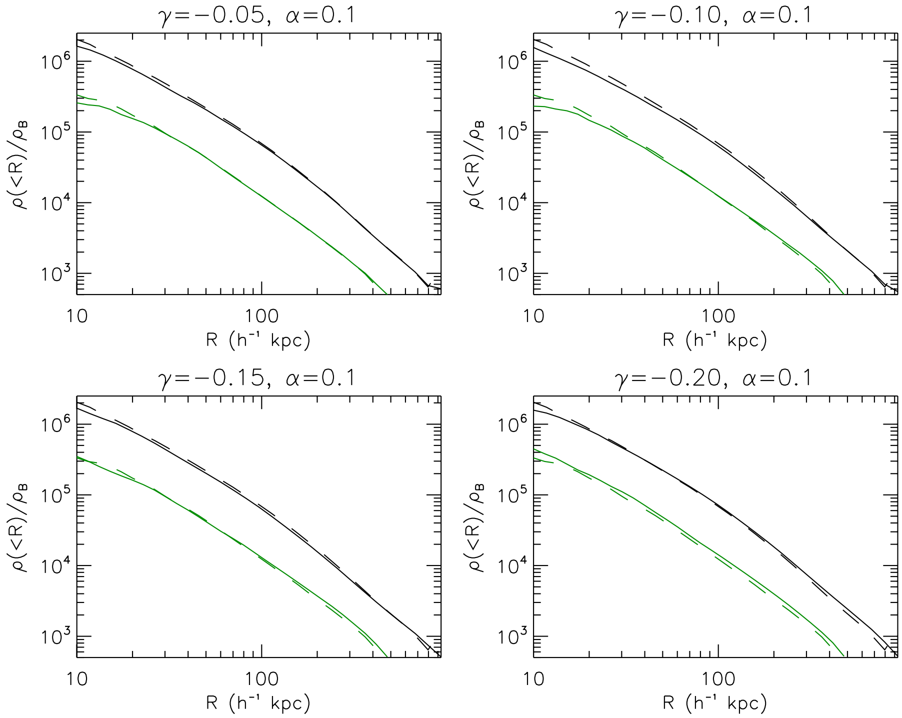

FIG. 12 (color online). The internal density profiled of two selected halos (see text) at $a = 1$. The four panels are for the four models we have simulated, as illustrated by the subtitles. In all panels solid curves are for the coupled-scalar-field model and dashed curves for ΛCDM. The upper (black) curves are result for halo I and the lower (green) curves for halo II.

$$\frac{\rho(r)}{\rho_c} = \frac{\beta}{\frac{r}{R_s}(1 + \frac{r}{R_s})^2} \tag{40}$$

where ρ_c is the critical density for matter, β is a dimensionless fitting parameter, and R_s a second fitting parameter with dimension of length; β and R_s are generally different for different halos and should be fitted for individual halos, but the formula in Eq. (40) is quite universal. Here we want to check whether the NFW formula can also describe the halos in our coupled-scalar-field simulations. Figure 13 shows the fitted concentration parameter $c_{\mathrm{NFW}} = r_{200}/R_s$, where r_200 is the radius at which the density is equal to 200 times the critical density ρ_c and R_s the NFW parameter, as well as the fitting error. The results show that the NFW profile can describe the halos from coupled-scalar-field simulations as well as it does in the ΛCDM simulations. The results show that c_{NFW} is smaller for the coupled-scalar-field models than for ΛCDM, but the difference is very small, which is consistent with Fig. 12.

Next, we can look at the bias between baryons and dark matter in the halos, which is displayed in Fig. 14. As expected, we find that the dark-matter density is constantly higher than that of baryons, due to the extra force they feel (note that other factors, such as the cosmic expansion rate and the modification of the source term in the Poisson equation, have the same influence on dark matter and baryons). In general, the bias increases with the coupling strength $|\gamma|$ which is easy to understand.

V. DISCUSSIONS

Before concluding the paper, we would like to have a discussion about the tests and resolution issues.

Our simulations have been performed using a modified version of the publicly available code MLAPM. To be clearer, we can divide the modified MLAPM code into two parts: the first is the default code, and the second includes all those new routines we have added to implement the computation of the scalar field and the fifth force etc.

We have done various direct and indirect tests for the second part: (a) The nonlinear Gauss-Seidel routines to solve the scalar field have been directly tested in a parallel work [49] for an analytically tractable case, and we find that the numerical solution agrees with the analytic one to a high precision. (b) For the models studied in this paper, we have found that the scalar-field perturbation is proportional to the gravitational potential (Figs. 7 and 8) to good accuracy, which shows the closeness to what one would obtain analytically (because in our models the scalar-field potential can be neglected in both the Poisson equation and the scalar-field equation of motion, so the two have proportional source terms). (c) The fifth force is also proportional to gravity (Fig. 6) to high precision, again in agreement with analytical expectations. (d) The matter power spectra agree with linear perturbation computation on large scales (Fig. 9). (e) The age of the Universe agrees with the result from the CAMB code and the integration using the MAPLE software. In summary, our additions to the MLAPM code

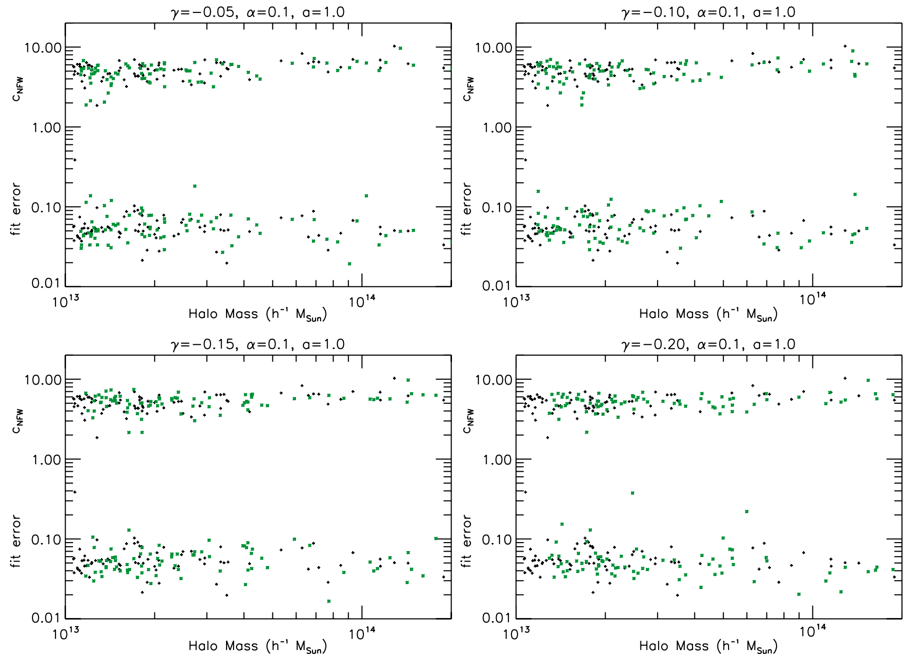

FIG. 13 (color online). The fit to the NFW density profile for the coupled-scalar-field models [asterisks (green)], as compared with that for the ΛCDM model [plus signs (black)]. The four panels are for the four models we are simulating. In each panel the upper points show the concentration parameter from the fitting, and the lower points show the fitting error. Each cross represents one halo and we have shown the 80 most massive halos from each simulation box.

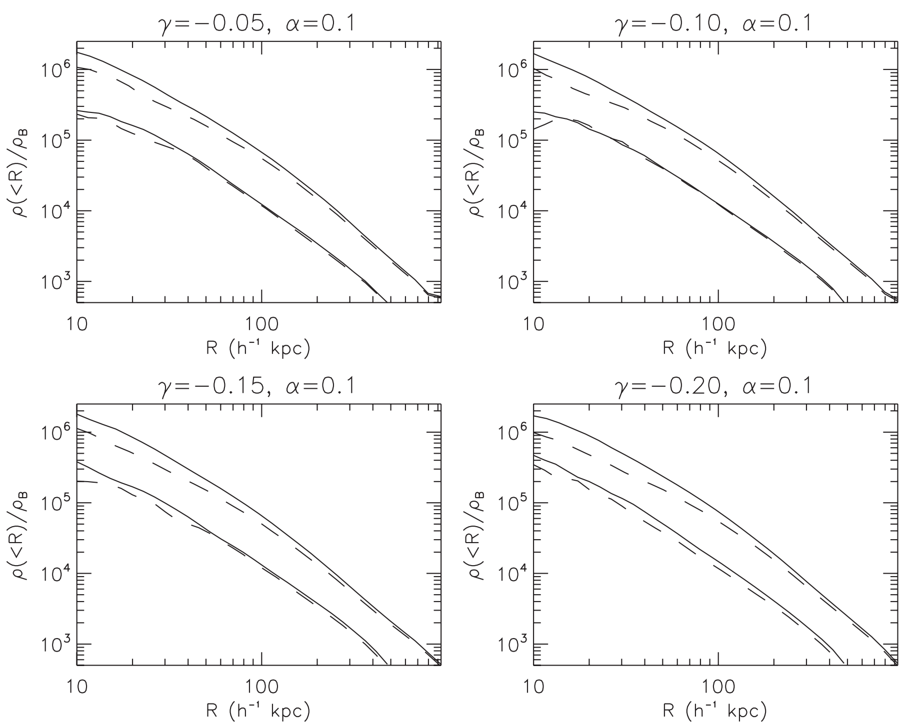

FIG. 14. The internal density profiles for dark matter (solid curves) and baryons (dashed curves) separately. We show this for the four models we have simulated, as indicated by the subtitles. In each panel the upper two curves are for halo I and the lower two curves for halo II.

have been tested in various ways and we find them to pass these tests.

For the mass resolution, we have two densities in our simulations, one for dark-matter particles and the other for baryons. In the usual particle-mesh simulations, the particle number is chosen to be the same as the number of grid cells (or $1/8$ of the latter). In our simulations, as we mentioned above, we found that these choices of particle number did not guarantee convergence of the scalar-field solver, and as a result we had to choose 256^3 particles rather than 128^3.[7] But these are all really only relevant for our scalar-field solver which, as mentioned above, does produce reliable results. Once the fifth force is obtained (and as we have seen it is proportional to gravity to a very good approximation), the remainder of the code is the same as the default MLAPM, which has been tested extensively in the code paper [42]. In any case, our mass resolution for the Poisson equation is higher than the value used in most PM simulations in the literature (with the same size of simulation box): we cannot lower it if we want the scalar-field solver to converge, and to increase it further seems to be unnecessary.

For the time stepping, the MLAPM code uses a self-adaptive time-stepping scheme, which means that the time step is adjusted according to the speed of particles so that no particles move farther than $1/5$ of the cell size in a given time step. In the scalar-field simulations, the time step is already smaller than in ΛCDM, because particles move faster than in ΛCDM because of the fifth force. For example, in the $\gamma = -0.2$ simulation more than 600 time steps are used from redshift 49 to today, and in ΛCDM about 400 are used. Again, since our modification to the code is confined to the scalar field and fifth force parts, the effects of choosing different numbers of time steps are only up to the original code. The code paper [42] compared two simulations with 250 and 400 time steps, respectively, and found that the resulting mass functions and matter power spectra are almost identical, and are very close to the results from other numerical codes.

For the spatial resolution, one of the important effects of grid size is on finding an accurate solution to the scalar field. In our models, the issue is not so important because, as we have seen, our grid size is fine enough to compute the fifth force accurately (compatible with analytical expectations). Because the fifth force is shown to be proportional to gravity, and thus the model is simply a ΛCDM one with a modified background expansion rate and rescaled Newtonian constant, we can use the test of the default MLAPM code to gain some idea about the effects of the spatial resolution. The test of the code paper [42] shows that doubling the spatial resolution only changes the matter power spectrum and mass function slightly. Also, we have tested the MLAPM code using 128^3 grid cells for three simulation boxes with sizes 128, 64, and $32h^{-1}$ Mpc, respectively, and the results show that their matter power spectra agree reasonably down to $k = 20h\ \mathrm{Mpc}^{-1}$, and then the results for the later two simulations agree further down to 30–$40h\ \mathrm{Mpc}^{-1}$. Unlike in the pure PM runs, where it is easy to determine down to what scale (the one related to the Nyquist frequency) the result remains reliable, it is more difficult to say this definitely for our self-adaptive runs. However, the tests mentioned above indicate that, conservatively, the result could be trusted down to $k = 20h\ \mathrm{Mpc}^{-1}$. Much higher-resolution simulations are too time consuming for the coupled-scalar-field models and will be left for future work.

VI. SUMMARY AND CONCLUSION

Couplings between any scalar field and (some of) the matter species can affect cosmology in various ways. There are two principal effects: modified source terms in the gravitational field equations (*channel I*) and direct new interactions between particles of the coupled matter species (*channel II*).

The effects through channel II arise in an inhomogeneous universe, but not in background cosmology. In principle, there is only an effect of this sort—the fifth force, due to the exchanges of scalar quanta between matter particles. In practice, (e.g., in N-body simulations), the scalar field φ is computed in the fundamental observer's frame while the fifth force must be evaluated in individual particle frames; consequently, the fifth force is split into two parts: the part from the spatial gradient of the scalar field $\delta\varphi$ in the fundamental observer's frame (which is independent of the particle's peculiar velocity v) and the part due to frame transformation which is proportional to v. In a homogeneous universe, there is no spatial gradient and all matter particles are comoving with the fundamental observers, so $v = 0$, and therefore the channel II effects vanish. In an inhomogeneous universe both terms are nonzero in general, leading to a net force which strengthens the attraction between particles, and enhances their gravitational clustering.

The effects arising through channel I appear both in homogeneous (via the Friedmann and Raychaudhuri equations) and inhomogeneous (via the Poisson equation) universes. They arise mainly via a renormalization of the contributions to the total density from the coupled matter species and by a new contribution from the scalar field itself. The exact effects depend on the specific forms of the scalar potential and coupling function. Here, we list our main findings for an inverse power-law potential Eq. (11), with an exponential coupling Eq. (12), and the model parameters given in Sec. III A.

For the background cosmology, the contribution to the Friedmann equation from dark matter is renormalized by

[7]Another reason to have more particles than usual is that the code here is self-adaptive and refines itself in high-density regions, so that having more particles helps avoid too low-mass resolutions on the refinements.

$C(\varphi) < 1$, and $C(\varphi)$ decreases as the coupling constant $|\gamma|$ increases. As a result, a stronger coupling (larger $|\gamma|$) produces a lower cosmic expansion rate during the matter-dominated era (Fig. 1),[8] which will in turn helps enhance the clustering of matter and promotes structure formation.

Such an enhancement is just what we have observed from our linear perturbation analysis (Figs. 2 and 3): on very large scales, which are beyond the range of the fifth force effects, the matter power spectrum increases with $|\gamma|$. On small scales, the fifth force helps to enhance the matter power, making it increase further than predicted in ΛCDM (comparing the left to the right panels of Fig. 3, where we have separated baryons, which have no scalar coupling, from dark matter, which has). This enhancement starts rather early, and so the scalar field does leave imprints on the matter power spectrum at $z \sim 50$, which means that the initial condition for N-body simulations also needs to modified. For example, in the model with $|\gamma| = 0.15$, we have found that :

(i) The density perturbation at $z \sim 49$ is about 10% larger than the corresponding result in ΛCDM for baryons (due to slower cosmic expansion) and about 12% larger for dark matter (due to the slower expansion *and* the fifth force effects).

(ii) The average velocity at the same time is about 8% larger than the corresponding result in ΛCDM for baryons and about 10% larger for dark matter. We introduce a quick method to take these changes into account when generating initial conditions for N-body simulations.

One of the most important results from our N-body simulations is the magnitude of fifth force. Figure 6 shows that everywhere and at any time (i.e., in both high and low density regions) the fifth force (or more precisely, the velocity-*independent* part of it) is proportional to gravity in magnitude (with a coefficient $2\gamma^2$ when only considering dark matter). This is the approximation used in many previous simplified simulations, and our results confirm numerically that this approximation works fairly well, at least for those cases where the scalar potential is unimportant, such as ours. We emphasize, however, that the velocity-dependent part of the fifth force should *not* be dropped (as in some previous simulations) unless there is good reason to do so (see [22]).

For the nonlinear matter power spectrum (Fig. 9), we find that the N-body simulations show agreement with linear perturbation analysis on large scales. On intermediate scales, our simulations predict significant enhancement in the matter power over that predicted both by linear perturbation analysis and by the ΛCDM paradigm. This enhancement is strongest at early epochs but gradually weakens at late times. One possible reason for this is that the scalar coupling, $C(\varphi)$, decreases with time, and reduces the contribution of dark matter to the gravitational potential, so weakening further clustering, but this still needs to be investigated in more detail.

The bias between dark matter and baryons increases with time and with coupling strength $|\gamma|$. This is because larger $|\gamma|$ implies stronger fifth forces and therefore stronger total forces act on dark-matter particles compared to baryons. As time passes, the bias has more time to develop and so increases as well (Fig. 10). Using the same reasoning, the fifth force increases the attraction of dark-matter particles and so heavier halos are expected to form during the structure formation (Fig. 11). In order to identify gravitationally bound and virialized halos in our models we must also take into account this scalar coupling (Sec. IV D).

The scalar-field coupling also has impacts on the internal density profiles of the halos (Figs. 12 and 13). We average ten of the heaviest halos and find:

(i) When compared with ΛCDM, the overdensities in the inner regions can be lower while those in the outer regions higher, showing the failure of the halos to retain particles in the inner region, either because the particles move too fast or because the attractive potential at the center is too weak.

(ii) The suppression of inner density compared with ΛCDM weakens, rather than strengthens, as $|\gamma|$ increases. Indeed, for $|\gamma| = 0.2$ the density is higher than ΛCDM result throughout the halos. More detailed studies are needed to clarify the leading effect responsible for this observed pattern.

(iii) There is a bias between density profiles for baryons and dark matter (Fig. 14): the dark-matter density is always higher because it experiences the fifth force which boosts its clustering.

In summary, in this paper we have been given a comprehensive description of the methodology and implementation of general N-body simulations for coupled-scalar-field models. As far as we know, this is the first time that some important issues in such simulations, such as the consistent solution of the scalar field and fifth force, the fifth force effect in generating initial conditions, the effect of scalar field on identifying virialized halos, etc. have been taken into account. Although the situation is complex, we have identified interesting new features in these models. It is our hope to see more fully developed results for the nonlinear structure formation in this class of models and their subsequent confrontation with observational data.

ACKNOWLEDGMENTS

The work described in this paper has been performed on COSMOS, the UK National Cosmology Supercomputer. The coding work at an early stage was done on the SARA

[8]Note in Fig. 1 (lower left panel) the expansion rate of the coupled-scalar-field model finally catches up with that of ΛCDM at $a = 1$. This is because at late times the dark-energy (scalar-field) density is higher than that in ΛCDM.

Supercomputer in the Netherlands, under the HPC-EUROPA2 project, with the support of the European Community Research Infrastructure Action under the FP8 Programme. The linear perturbation calculations in this work are performed using CAMB [52]. We thank Luca Amendola, Marco Baldi, Kazuya Koyama, Andrea Maccio, Gong-Bo Zhao, and Hongsheng Zhao for useful conversations relevant to this work, and the computing staff of DAMTP for technical help in the usage of COSMOS. B. Li is supported by Queens' College, Cambridge, and the STFC.

APPENDIX A: DISCRETIZED EQUATIONS FOR THE N-BODY SIMULATIONS

In the MLAPM code for Poisson equation (28) is [and in our modified code the scalar-field equation of motion Eq. (29) will also be] solved on discretized grid points, so we must develop the discrete versions of Eqs. (26)–(29) to be implemented in the code. First, we write down the full formalism of the relevant equations.

Introducing the variable u (cf. Sec. II C), the Poisson equation becomes

$$\begin{aligned}\nabla^2\Phi_c = {}& \frac{3}{2}\Omega_{\rm CDM}\left\{\rho_{c,\rm CDM}\exp\left[\gamma\left(\sqrt{\kappa}\bar{\varphi}+\frac{B^2H_0^2}{ac^2}u\right)\right]\right.\\ &\left. - e^{\gamma\sqrt{\kappa}\bar{\varphi}}\right\} + \frac{3}{2}\Omega_{\rm B}(\rho_{c,\rm B}-1)\\ &- \frac{3\lambda a^3}{[\sqrt{\kappa}\bar{\varphi}+\frac{B^2H_0^2}{ac^2}u]^{\alpha}} + \frac{3\lambda a^3}{[\sqrt{\kappa}\bar{\varphi}]^{\alpha}},\end{aligned} \tag{A1}$$

where λ is defined in Eq. (30) and is a constant of $O(1)$ (actually $\lambda \sim \Omega_{\rm DE}$ where DE means dark energy). Its value and that of the quantity $\sqrt{\kappa}\bar{\varphi}$ are determined solely by the background evolution. The computation of the background quantities is discussed in Sec. III C.

The scalar-field equation of motion now becomes

$$\begin{aligned}\nabla^2 u = {}& 3\gamma\Omega_{\rm CDM}\rho_{c,\rm CDM}\exp\left[\gamma\left(\sqrt{\kappa}\bar{\varphi}+\frac{B^2H_0^2}{ac^2}u\right)\right]\\ &- \frac{3\alpha\lambda a^3}{[\sqrt{\kappa}\bar{\varphi}+\frac{B^2H_0^2}{ac^2}u]^{1+\alpha}} - 3\gamma\Omega_{\rm CDM}e^{\gamma\sqrt{\kappa}\bar{\varphi}}\\ &+ \frac{3\alpha\lambda a^3}{[\sqrt{\kappa}\bar{\varphi}]^{1+\alpha}}.\end{aligned} \tag{A2}$$

So, in terms of the new variable u, the set of equations used in the N-body code is Eqs. (26) and (27) plus Eqs. (A1) and (A2). These equations were used in the code. Among them, Eqs. (A1) and (27) will use the value of u, while Eq. (A2) solves for u. In order that these equations can be integrated into MLAPM, we need to discretize Eq. (A2) for the application of the Newton-Gauss-Seidel relaxation method. This involves writing down a discrete version of this equation on a uniform grid with grid spacing h. Suppose we want to achieve second-order precision, as is in the default Poisson solver of MLAPM, then $\nabla^2 u$ in one dimension can be written as

$$\nabla^2 u \to \nabla^{h2}u_j = \frac{u_{j+1}+u_{j-1}-2u_j}{h^2} \tag{A3}$$

where a subscript j means that the quantity is evaluated on the jth point. The generalization to three dimensions is straightforward.

The discrete version of Eq. (A2) is

$$L^h(u_{i,j,k}) = 0, \tag{A4}$$

in which

$$\begin{aligned}L^h(u_{i,j,k}) = {}& \frac{1}{h^2}[u_{i+1,j,k}+u_{i-1,j,k}+u_{i,j+1,k}+u_{i,j-1,k}+u_{i,j,k+1}+u_{i,j,k-1}-6u_{i,j,k}]\\ &- \left[3\gamma\Omega_{\rm CDM}\rho_{c,\rm CDM}\exp\left[\gamma\left(\sqrt{\kappa}\bar{\varphi}+\frac{B^2H_0^2}{ac^2}u_{i,j,k}\right)\right] - \frac{3\alpha\lambda a^3}{[\sqrt{\kappa}\bar{\varphi}+\frac{B^2H_0^2}{ac^2}u_{i,j,k}]^{1+\alpha}}\right]\\ &+ \left[3\gamma\Omega_{\rm CDM}e^{\gamma\sqrt{\kappa}\bar{\varphi}} - \frac{3\alpha\lambda a^3}{[\sqrt{\kappa}\bar{\varphi}]^{1+\alpha}}\right].\end{aligned} \tag{A5}$$

Then, the Newton-Gauss-Seidel iteration says that we can obtain a new (and often more accurate) solution of u, $u^{\rm new}_{i,j,k}$, using our knowledge about the old (and less accurate) solution $u^{\rm old}_{i,j,k}$ via

$$u^{\rm new}_{i,j,k} = u^{\rm old}_{i,j,k} - \frac{L^h(u^{\rm old}_{i,j,k})}{\partial L^h(u^{\rm old}_{i,j,k})/\partial u_{i,j,k}}. \tag{A6}$$

The old solution will be replaced by the new solution to $u_{i,j,k}$ once the new solution is ready, using the red-black Gauss-Seidel sweeping scheme. Note that

$$\begin{aligned}\frac{\partial L^h(u_{i,j,k})}{\partial u_{i,j,k}} = {}& -\frac{6}{h^2} - 3\gamma^2\frac{(H_0B)^2}{ac^2}\Omega_{\rm CDM}\rho^{\rm CDM}_{c,i,j,k}\\ &\times\exp\left[\gamma\left(\sqrt{\kappa}\bar{\varphi}+\frac{B^2H_0^2}{ac^2}u_{i,j,k}\right)\right]\\ &- \frac{(H_0B)^2}{ac^2}\frac{3\alpha(1+\alpha)\lambda a^3}{[\sqrt{\kappa}\bar{\varphi}+\frac{B^2H_0^2}{ac^2}u_{i,j,k}]^{2+\alpha}}.\end{aligned} \tag{A7}$$

In principle, if we start from a high redshift, then the initial guess of $u_{i,j,k}$ for the relaxation could be so chosen that the initial value of φ in all space is equal to the background value $\bar{\varphi}$, because at this time we expect this to be approximately true any way. At subsequent time steps we could use the solution for $u_{i,j,k}$ from the previous time step as our initial guess. If the time step is small enough then we would expect u to change only slightly between consecutive time steps so that such a guess will be good enough for the iterations to converge quickly.

In practice, however, due to specific features and the algorithm of the MLAPM code [42], the above procedure may be slightly different in details.

APPENDIX B: ABOUT THE DARK-MATTER LAGRANGIAN

For simplicity, let us write the Lagrangian as $\mathcal{L}_{\rm CDM} = F^{1/2} = \sqrt{g_{ab}\dot{x}^a\dot{x}^b}$ [i.e., neglecting the mass term and δ-function term in Eq. (2)] in which $\dot{x}^a \equiv dx^a/ds$ and s is some general parametrization of the particle's geodesics (we only use this definition in this appendix and note that in other places $\dot{x}$ has different meaning). The Euler-Lagrange equation is

$$\frac{d}{ds}\frac{\partial \mathcal{L}{\rm CDM}}{\partial \dot{x}^a} = \frac{\partial \mathcal{L}_{\rm CDM}}{\partial x^a} \tag{B1}$$

in which we have

$$\begin{aligned}\frac{\partial \mathcal{L}_{\rm CDM}}{\partial x^a} &= \frac{1}{2}F^{-1/2}g_{bc,a}\dot{x}^b\dot{x}^c,\\ \frac{\partial \mathcal{L}_{\rm CDM}}{\partial \dot{x}^a} &= \frac{1}{2}F^{-1/2}\frac{\partial}{\partial \dot{x}^a}(g_{bc}\dot{x}^b\dot{x}^c)\\ &= \frac{1}{2}F^{-1/2}g_{bc}(\delta^b_a\dot{x}^c + \delta^c_a\dot{x}^b),\end{aligned}$$

and

$$\frac{d}{ds}\frac{\partial \mathcal{L}_{\rm CDM}}{\partial \dot{x}^a} = F^{-1/2}\Big[g_{ab}\ddot{x}^b - \frac{1}{2}F^{-1}\dot{F}g_{ab}\dot{x}^b + \frac{1}{2} \times (g_{ac,b}\dot{x}^b\dot{x}^c + g_{ab,c}\dot{x}^b\dot{x}^c)\Big]$$

so that the Lagrange equation becomes

$$\ddot{x}^d - \tfrac{1}{2}F^{-1}\dot{F}\dot{x}^d + \Gamma^d_{bc}\dot{x}^b\dot{x}^c = 0. \tag{B2}$$

For timelike geodesics we can choose $s = \tau$ (τ being the proper time) which means that $F = 1$ so that Eq. (B2) becomes the conventional geodesic equation

$$\ddot{x}^a + \Gamma^a_{bc}\dot{x}^b\dot{x}^c = 0. \tag{B3}$$

If $F \neq 1$ then we will have to stick to Eq. (B2) as the geodesic equation, which is not what we are familiar with. We could note that $F = 1$ (and $\mathcal{L}_{\rm CDM} = 1$ above) corresponds to the result in our Eq. (4).

As it stands, Eq. (4) is exact. Because we use proper time τ for s, so the geodesic equation is also written in terms of τ, which means that when we switch from τ to the physical time t in Eq. (16) there will be some approximation, but Eq. (16) is approximate anyway.

APPENDIX C: AN ALGORITHM TO SOLVE FOR THE BACKGROUND EVOLUTION

Here, we aim to give the formulas and an algorithm for the background field equations which can also be applied to linear Boltzmann codes such as CAMB. Throughout this appendix we use the conformal time τ instead of the physical time t, and $' \equiv d/d\tau$, $\mathcal{H} \equiv a'/a$. All quantities appearing here are background ones unless stated otherwise.

For convenience, we will work with dimensionless quantities and define $\tilde{\varphi} \equiv \sqrt{\kappa}\varphi$ and $N \equiv \ln a$ so that

$$\tilde{\varphi}' = \mathcal{H}\frac{d\tilde{\varphi}}{dN}, \tag{C1}$$

$$\tilde{\varphi}'' = \mathcal{H}^2\frac{d^2\tilde{\varphi}}{dN^2} + \mathcal{H}'\frac{d\tilde{\varphi}}{dN}. \tag{C2}$$

With these definitions it is straightforward to show that Eq. (31) can be expressed as

$$\Big(\frac{\mathcal{H}}{\mathcal{H}_0}\Big)^2\frac{d^2\tilde{\varphi}}{dN^2} + \Big(2\frac{\mathcal{H}^2}{\mathcal{H}_0^2} + \frac{\mathcal{H}'}{\mathcal{H}_0^2}\Big)\frac{d\tilde{\varphi}}{dN} - 3\alpha\lambda a^2\frac{1}{\tilde{\varphi}^{1+\alpha}} + \frac{3}{a}\gamma\Omega_{\rm CDM}e^{\gamma\tilde{\varphi}} = 0, \tag{C3}$$

where $\mathcal{H}_0$ is the current value of $\mathcal{H}$, and the coefficients of the derivative terms are given by Eqs. (32) and (33) as

$$\Big(\frac{\mathcal{H}}{\mathcal{H}_0}\Big)^2 = \frac{\Omega_{\rm RAD}a^{-2} + \Omega_{\rm B}a^{-1} + e^{\gamma\tilde{\varphi}}\Omega_{\rm CDM}a^{-1} + \frac{\lambda a^2}{\tilde{\varphi}^\alpha}}{1 - \frac{1}{6}(\frac{d\tilde{\varphi}}{dN})^2}, \tag{C4}$$

and

$$\frac{\mathcal{H}'}{\mathcal{H}_0^2} = -\frac{1}{3}\Big(\frac{d\tilde{\varphi}}{dN}\Big)^2\frac{\mathcal{H}^2}{\mathcal{H}_0^2} + \frac{\lambda a^2}{\tilde{\varphi}^\alpha} - \Big[\Omega_{\rm RAD}a^{-2} + \frac{1}{2}\Omega_{\rm B}a^{-1} + \frac{1}{2}e^{\gamma\tilde{\varphi}}\Omega_{\rm CDM}a^{-1}\Big]. \tag{C5}$$

In all of the above equations we have used the facts that

$$\rho_{\rm CDM} \propto a^{-3}, \qquad \rho_{\rm B} \propto a^{-3}, \qquad \rho_{\rm RAD} \propto a^{-4}.$$

We stress again that although coupled to the scalar field, the background dark-matter energy density follows the same conservation law as in ΛCDM. The effect of the coupling is reflected in the fact that there is a coefficient $e^{\gamma\tilde{\varphi}}$ in front of $\Omega_{\rm CDM}$ whenever the latter appears in the gravitational equations or the scalar-field evolution equation [20].

When solving for φ (or $\tilde{\varphi}$), we just use Eq. (C3) aided by Eqs. (C4) and (C5). It may appear then that, given any initial values for $\tilde{\varphi}_{\rm ini}$ and $(d\tilde{\varphi}/dN)_{\rm ini}$, the evolution of φ is obtainable. However, Eq. (C4) is not necessarily satisfied for $\tilde{\varphi}$ evolved in such way. Instead, it constrains that the initial condition $\tilde{\varphi}$ must start with, and the way it must subsequently evolve. This in turn is determined by the parameters λ, α, γ; since α, γ specify a model and are fixed once the model is chosen, the only concern is λ.

For the initial conditions $\tilde{\varphi}_{\rm ini}$ and $(d\tilde{\varphi}/dN)_{\rm ini}$, we have found that the subsequent evolution of $\tilde{\varphi}$ is rather insensitive to them. Thus, we choose $\tilde{\varphi}_{\rm ini} = (d\tilde{\varphi}/dN)_{\rm ini} = 0$ at some very early time (say $N_{\rm ini}$ corresponds to $a_{\rm ini} = e^{N_{\rm ini}} = 10^{-6}$) in all the models. Such a choice is clearly not only practical but also reasonable, given the fact that we expect that the scalar field starts high up the potential and rolls down subsequently.

As for λ, we use a trial-and-error method to find its value which ensures that (here a subscript 0 denotes the present-day value)

$$\Omega_{\rm RAD} + \Omega_{\rm B} + e^{\gamma\tilde{\varphi}_0}\Omega_{\rm CDM} + \frac{\lambda}{\tilde{\varphi}_0^{\alpha}} = 1 - \frac{1}{6}\left(\frac{d\tilde{\varphi}}{dN}\right)_0^2$$

which comes from setting $a = 1$ in Eq. (C4).

We determine the correct value of λ for any given α, γ in this way using MAPLE, and then compute the values of $\tilde{\varphi}$ and $d\tilde{\varphi}/dN$ for predefined values of N stored in an array. Their values at any time are then obtained using interpolation, and with these it is straightforward to compute other relevant quantities, such as $\mathcal{H}$, $\mathcal{H}'$, and φ, which are used in the Boltzmann and N-body codes.

APPENDIX D: THE ZELDOVICH APPROXIMATION

The initial conditions for N-body simulations are conventionally generated using the Zeldovich approximation [50,51], which in its original form works only for noncoupled dark matter. When there is a nonminimal coupling between dark-matter particles and a scalar field, it must be generalized, and we discuss this here.

Consider a particle whose actual position $\mathbf{r}$ is given as

$$\mathbf{r} = a(t)\mathbf{q} + b(t)\mathbf{d} \tag{D1}$$

where $\mathbf{q}$ is the Lagrangian coordinate (i.e., initial comoving coordinate with displacement), $\mathbf{d}$ is the displacement from $\mathbf{q}$ and $b(t)$ governs how the displacement increases in time (or, equivalently, how the density perturbation grows). From this, we have a deformation tensor

$$\mathcal{D}_{ij} = \frac{\partial r_i}{\partial q_j} = a(t)\delta_{ij} + b(t)\frac{\partial d_i}{\partial q_j}, \tag{D2}$$

which is just the Jacobian of the coordinate transformation, providing information about the change of the size of a given volume element (centered on the particle). When the deformation is small, as in the case of the early times when we set up the initial condition, we have

$$\det\mathcal{D} \doteq a^3(t)\left[1 + \frac{b}{a}\nabla_{\mathbf{q}}\cdot\mathbf{d}\right] \tag{D3}$$

where we have neglected higher-order terms in $\mathbf{d}$, and $\nabla_{\mathbf{q}}$ is the spatial derivative with respect to the Lagrangian coordinate $\mathbf{q}$. Note that the term in brackets is the fractional change of the volume element due to the collapse of matter.

In a given volume element, because we have two matter species now and their density contrasts grow at different rates because of the different scalar-field coupling, it makes sense to have two different $'b(t)'$ functions: $b(t)$ for baryons and $\tilde{b}(t)$ for dark matter. Thus, we end up with

$$\mathbf{r}_{\rm B} = a\mathbf{q} + b\mathbf{d}, \tag{D4}$$

$$\mathbf{r}_{\rm D} = a\mathbf{q} + \tilde{b}\mathbf{d}, \tag{D5}$$

in which $\mathbf{r}_{\rm B}$, $\mathbf{r}_{\rm D}$ denote the actual positions of a baryonic particle and a dark-matter particle residing in the volume element. We now want to solve for b and $\tilde{b}$.

As we will work with constant dark-matter mass, the mass conservation is just as simple as in ΛCDM, and, assuming no particles escape or enter our volume element, we have

$$\bar{\rho}_{\rm B}(t)a^3d^3\mathbf{q} = \rho_{\rm B}(t,\mathbf{r})d^3\mathbf{r}, \tag{D6}$$

$$\bar{\rho}_{\rm D}(t)a^3d^3\mathbf{q} = \rho_{\rm D}(t,\mathbf{r})d^3\mathbf{r}, \tag{D7}$$

where $\bar{\rho}$ is the average density. Now, from Eq. (D3), it follows directly that

$$\rho_{\rm B}(t,\mathbf{r}) = \frac{\bar{\rho}_{\rm B}(t)a^3}{\det\mathcal{D}} \doteq \bar{\rho}_{\rm B}(t)\left[1 - \frac{b}{a}\nabla_{\mathbf{q}}\cdot\mathbf{d}\right], \tag{D8}$$

$$\rho_{\rm D}(t,\mathbf{r}) = \frac{\bar{\rho}_{\rm D}(t)a^3}{\det\mathcal{D}} \doteq \bar{\rho}_{\rm D}(t)\left[1 - \frac{\tilde{b}}{a}\nabla_{\mathbf{q}}\cdot\mathbf{d}\right] \tag{D9}$$

and so the density contrasts can be expressed in terms of b and $\tilde{b}$ as

$$\delta_{\rm B} = -\frac{b}{a}\nabla_{\mathbf{q}}\cdot\mathbf{d} \equiv -D_+\nabla_{\mathbf{q}}\cdot\mathbf{d}, \tag{D10}$$

$$\delta_{\rm D} = -\frac{\tilde{b}}{a}\nabla_{\mathbf{q}}\cdot\mathbf{d} \equiv -\tilde{D}_+\nabla_{\mathbf{q}}\cdot\mathbf{d}, \tag{D11}$$

where D_+, $\tilde{D}_+$ will be identified as the linear growth factors for baryons and dark matter below.

Now consider the force laws obeyed by baryons and dark matter. For baryons this is very simple. In the Newtonian limit:

$$\ddot{\mathbf{r}}_{\rm B} = -\nabla_{\mathbf{r}}\phi \tag{D12}$$

where $\nabla_{\mathbf{r}}$ is the spatial derivative with respect to $\mathbf{r}$, and we have

$$\nabla_{\mathbf{q}} \doteq a\nabla_{\mathbf{r}} \tag{D13}$$

in the limit of small $\mathbf{d}$. Here, ϕ is the gravitational potential given by

$$\nabla_{\mathbf{r}}^2\phi \doteq 4\pi G[\rho_{\rm B} + e^{\gamma\varphi}\rho_{\rm D} - 2V(\varphi)], \quad \text{(D14)}$$

where we have neglected the radiation, which is negligible at later times, and the kinetic energy of the scalar field φ, which is always small. Meanwhile, the force law for dark-matter particles has a contribution from the scalar-field coupling:

$$\ddot{\mathbf{r}}_{\rm D} = -\nabla_{\mathbf{r}}\phi + \gamma\nabla_{\mathbf{r}}\varphi \quad \text{(D15)}$$

where in case that the scalar-field potential $V(\varphi)$ is flat (as in our case) and the perturbation to the scalar field φ is small (for redshift $z \gtrsim 50$), the scalar-field equation of motion is approximately

$$\nabla_{\mathbf{r}}^2\varphi \doteq 8\gamma\pi G e^{\gamma\varphi}(\rho_{\rm D} - \bar{\rho}_{\rm D}). \quad \text{(D16)}$$

Writing $\nabla = \nabla_{\mathbf{r}}$ from here on, and neglecting the perturbation in φ and $V(\varphi)$, from Eqs. (D10) and (D14) we have

$$\begin{aligned}\nabla^2\phi &= 4\pi G[\bar{\rho}_{\rm B} + e^{\gamma\varphi}\bar{\rho}_{\rm D} - 2\bar{V}(\varphi)] \\ &\quad - 4\pi G(\bar{\rho}_{\rm B}D_+ + e^{\gamma\varphi}\bar{\rho}_{\rm D}\tilde{D}_+)a\nabla\cdot\mathbf{d} \\ &= -3\frac{\ddot{a}}{a} - 4\pi G(\bar{\rho}_{\rm B}D_+ + e^{\gamma\varphi}\bar{\rho}_{\rm D}\tilde{D}_+)a\nabla\cdot\mathbf{d}\end{aligned}$$

where we have used the Raychaudhuri equation. This can be integrated once to obtain

$$\nabla\phi = -\frac{\ddot{a}}{a}\mathbf{r} - 4\pi G(\bar{\rho}_{\rm B}D_+ + e^{\gamma\varphi}\bar{\rho}_{\rm D}\tilde{D}_+)a\mathbf{d}. \quad \text{(D17)}$$

Equations (D4), (D12), and (D17) then give, after some algebra,

$$\ddot{D}_+ + 2\frac{\dot{a}}{a}\dot{D}_+ - 4\pi G[\bar{\rho}_{\rm B}D_+ + e^{\gamma\varphi}\bar{\rho}_{\rm D}\tilde{D}_+] = 0. \quad \text{(D18)}$$

This is the equation for b.

The idea of deriving the equation for $\tilde{b}$ is quite similar, but now we need to take into account the fifth force. Here, Eq. (D16) can be reexpressed, using Eq. (D11), as

$$\nabla^2\varphi = 8\pi G a\gamma e^{\gamma\varphi}\bar{\rho}_{\rm D}\tilde{D}_+\nabla\cdot\mathbf{d}$$

which can be integrated once to obtain

$$\nabla\varphi = 8\pi G a\gamma e^{\gamma\varphi}\bar{\rho}_{\rm D}\tilde{D}_+\mathbf{d}. \quad \text{(D19)}$$

Then, Eqs. (D5), (D15), (D17), and (D19) lead, again after some algebra, to

$$\ddot{\tilde{D}}_+ + 2\frac{\dot{a}}{a}\dot{\tilde{D}}_+ - 4\pi G[\bar{\rho}_{\rm B}D_+ + \beta e^{\gamma\varphi}\bar{\rho}_{\rm D}\tilde{D}_+] = 0, \quad \text{(D20)}$$

where we have defined $\beta \equiv 1 + 2\gamma^2$ to encode the effects of the fifth force.

Equations (D18) and (D20) indicate that D_+, $\tilde{D}_+$ are the linear growth factors of baryons and dark matter. Indeed, if the coupling constant $\gamma = 0$, then we find that $D_+ = \tilde{D}_+$ and

$$\ddot{D}_+ + 2\frac{\dot{a}}{a}\dot{D}_+ - 4\pi G\bar{\rho}_m D_+ = 0, \quad \text{(D21)}$$

where $\bar{\rho}_m = \bar{\rho}_{\rm B} + \bar{\rho}_{\rm D}$ is the total matter density. This is the familiar equation of the linear growth equation in this approximation.

In this discussion we have made several approximations. For example, the kinetic energy of the scalar field, which is always subdominant, is neglected; the perturbation of the scalar-field potential energy is also neglected since the scalar-field perturbation is small, especially at the time we set up the initial condition; the spatial dependence of $\tilde{D}_+$ is neglected implicitly, because we only consider small scales where the fifth force simply rescales the gravitational constant which governs structure growth.

Equations (D10) and (D11) are the starting point of the numerical codes which generate initial conditions for N-body simulations, such as GRAFIC2. Given the matter power spectrum at the initial time t_i, the code produces the density fluctuation field δ as a Gaussian random field and works out the displacement field $\mathbf{d}$, or actually $D_+\mathbf{d}$, because

$$\mathbf{r} = a\mathbf{q} + b\mathbf{d} = a(\mathbf{q} + D_+\mathbf{d}) \equiv a\mathbf{x}. \quad \text{(D22)}$$

The initial peculiar velocity of the particle is then

$$\mathbf{v} = a\dot{\mathbf{x}} = a\dot{D}_+\mathbf{d} \equiv f\frac{d\ln a}{d\tau}D_+\mathbf{d} \quad \text{(D23)}$$

where τ is the conformal time and

$$f \equiv \frac{d\ln D_+}{d\ln a}. \quad \text{(D24)}$$

In our model the initial displacements and velocities of particles should be generated separately for the two different matter species, using their respective matter power spectrum and linear growth factor D_+ (or $\tilde{D}_+$).

[1] E. J. Copeland, S. Sami, and S. Tsujikawa, Int. J. Mod. Phys. D **15**, 1753 (2006).
[2] C. Wetterich, Nucl. Phys. **B302**, 668 (1988).
[3] B. Ratra and P. J. E. Peebles, Phys. Rev. D **37**, 3406 (1988).
[4] R. R. Caldwell, R. Dave, and P. J. Steinhardt, Phys. Rev. Lett. **80**, 1582 (1998).
[5] L. Amendola, Phys. Rev. D **62**, 043511 (2000).
[6] R. Bean and J. Magueijo, Phys. Lett. B **517**, 177 (2001).
[7] L. Amendola, Phys. Rev. D **69**, 103524 (2004).

[8] T. Koivisto, Phys. Rev. D **72**, 043516 (2005).
[9] S. Lee, G. -C. Liu, and K. -W. Ng, Phys. Rev. D **73**, 083516 (2006).
[10] C. G. Boehmer, G. Caldera-Cabral, R. Lazkoz, and R. Maartens, Phys. Rev. D **78**, 023505 (2008).
[11] R. Bean, E. E. Flanagan, I. Laszlo, and M. Trodden, Phys. Rev. D **78**, 123514 (2008).
[12] R. Bean, E. E. Flanagan, and M. Trodden, Phys. Rev. D **78**, 023009 (2008).
[13] C. G. Boehmer, G. Caldera-Cabral, N. Chan, R. Lazkoz, and R. Maartens, Phys. Rev. D **81**, 083003 (2010).
[14] J. Khoury and A. Weltman, Phys. Rev. D **69**, 044026 (2004).
[15] D. F. Mota and D. J. Shaw, Phys. Rev. D **75**, 063501 (2007).
[16] P. Brax, C. van de Bruck, A. C. Davis, and D. J. Shaw, Phys. Rev. D **82**, 063519 (2010).
[17] G. Caldera-Cabral, R. Maartens, and B. M. Schaefer, J. Cosmol. Astropart. Phys. 07 (2009) 027.
[18] J. Valiviita, R. Maartens, and E. Majerotto, Mon. Not. R. Astron. Soc. **402**, 2355 (2010).
[19] F. Simpson, B. M. Jackson, and J. A. Peacock, arXiv:1004.1920.
[20] B. Li and H. Zhao, Phys. Rev. D **80**, 044027 (2009).
[21] H. Zhao, A. V. Maccio, B. Li, H. Hoekstra, and M. Feix, Astrophys. J. Lett. **712**, L179 (2010).
[22] B. Li and H. Zhao, Phys. Rev. D **81**, 104047 (2010).
[23] E. Bertschinger, Annu. Rev. Astron. Astrophys. **36**, 599 (1998).
[24] E. V. Linder and A. Jenkins, Mon. Not. R. Astron. Soc. **346**, 573 (2003).
[25] R. Mainini, A. V. Maccio, S. A. Bonometto, and A. Klypin, Astrophys. J. **599**, 24 (2003).
[26] V. Springel and G. R. Farrar, Mon. Not. R. Astron. Soc. **380**, 911 (2007).
[27] M. Kesden and M. Kamionkowski, Phys. Rev. Lett. **97**, 131303 (2006); Phys. Rev. D **74**, 083007 (2006).
[28] G. R. Farrar and R. A. Rosen, Phys. Rev. Lett. **98**, 171302 (2007).
[29] J. A. Keselman, A. Nusser, and P. J. E. Peebles, Phys. Rev. D **80**, 063517 (2009).
[30] A. V. Maccio, C. Quercellini, R. Mainini, L. Amendola, and S. A. Bonometto, Phys. Rev. D **69**, 123516 (2004).
[31] M. Baldi, V. Pettorino, G. Robbers, and V. Springel, Mon. Not. R. Astron. Soc. **403**, 1684 (2010).
[32] M. A. Rodriguez-Meza, A. X. Gonzalez-Morales, R. F. Gabbasov, and J. L. Cervantes-Cota, J. Phys. Conf. Ser. **91**, 012012 (2007).
[33] M. A. Rodriguez-Meza, AIP Conf. Proc. **1083**, 190 (2008).
[34] M. A. Rodriguez-Meza, AIP Conf. Proc. **1116**, 171 (2009).
[35] W. A. Hellwing and R. Juszkiewicz, Phys. Rev. D **80**, 083522 (2009).
[36] H. Oyaizu, Phys. Rev. D **78**, 123523 (2008).
[37] H. Oyaizu, M. Lima, and W. Hu, Phys. Rev. D **78**, 123524 (2008).
[38] I. Laszlo and R. Bean, Phys. Rev. D **77**, 024048 (2008).
[39] F. Schmidt, Phys. Rev. D **80**, 043001 (2009).
[40] K. C. Chan and R. Scoccimarro, Phys. Rev. D **80**, 104005 (2009).
[41] W. Cui, P. Zhang, and X. Yang, Phys. Rev. D **81**, 103528 (2010).
[42] A. Knebe, A. Green, and J. Binney, Mon. Not. R. Astron. Soc. **325**, 845 (2001).
[43] B. Li and J. D. Barrow (unpublished).
[44] S. Colombi, A. Jaffe, D. Novikov, and C. Pichon, Mon. Not. R. Astron. Soc. **393**, 511 (2009).
[45] M. Baldi and M. Viel, arXiv:1007.3736.
[46] S. P. D. Gill, A. Knebe, and B. K. Gibson, Mon. Not. R. Astron. Soc. **351**, 399 (2004).
[47] S. Knollmann and A. Knebe, Astrophys. J. Suppl. Ser. **182**, 608 (2009).
[48] J. F. Navarro, C. S. Frenk, and S. White, Astrophys. J. **462**, 563 (1996).
[49] G. Zhao, B. Li, and K. Koyama (unpublished).
[50] Ya. B. Zel'dovich, Astron. Astrophys. **5**, 84 (1970).
[51] G. Efstathiou, M. Davis, S. D. M. White, and C. S. Frenk, Astrophys. J. Suppl. Ser. **57**, 241 (1985).
[52] A. M. Lewis, A. Challinor, and A. Lasenby, Astrophys. J. **538**, 473 (2000).